

REPORT DOCUMENTATION PAGE				Form Approved OMB No. 0704-0188	
Public reporting burden for this collection of information is estimated to average 1 hour per response, including the time for reviewing instructions, searching existing data sources, gathering and maintaining the data needed, and completing and reviewing this collection of information. Send comments regarding this burden estimate or any other aspect of this collection of information, including suggestions for reducing this burden to Department of Defense, Washington Headquarters Services, Directorate for Information Operations and Reports (0704-0188), 1215 Jefferson Davis Highway, Suite 1204, Arlington, VA 22202-4302. Respondents should be aware that notwithstanding any other provision of law, no person shall be subject to any penalty for failing to comply with a collection of information if it does not display a currently valid OMB control number. PLEASE DO NOT RETURN YOUR FORM TO THE ABOVE ADDRESS.					
1. REPORT DATE (DD-MM-YYYY) 30/Nov/2006		2. REPORT TYPE Final Report		3. DATES COVERED (From - To) 01/Sep/2004 - 30/Nov/2006	
4. TITLE AND SUBTITLE  Innovative Methods for Engine Health Monitoring				5a. CONTRACT NUMBER	
				5b. GRANT NUMBER FA9550-04-1-0254	
				5c. PROGRAM ELEMENT NUMBER	
6. AUTHOR(S) C. L. Philip Chen, Z. Pantic-Tanner, H. Millwater, S. Hudak, Y. Huang, P. Cotae, D. Tanner, E. John, K. Chan, X. Wang				5d. PROJECT NUMBER	
				5e. TASK NUMBER	
				5f. WORK UNIT NUMBER	
7. PERFORMING ORGANIZATION NAME(S) AND ADDRESS(ES)  The University of Texas at San Antonio College of Engineering San Antonio, TX 78249				8. PERFORMING ORGANIZATION REPORT NUMBER	
9. SPONSORING / MONITORING AGENCY NAME(S) AND ADDRESS(ES) Air Force Office of Scientific Research Aerospace and Materials Sciences Structural Mechanics  <i>Dr. Victor Giurgutzu/NA</i>				10. SPONSOR/MONITOR'S ACRONYM(S) AFOSR/NA	
				11. SPONSOR/MONITOR'S REPORT NUMBER(S)	
12. DISTRIBUTION / AVAILABILITY STATEMENT Unlimited  <b>DISTRIBUTION STATEMENT A</b> Approved for Public Release Distribution Unlimited					
13. SUPPLEMENTARY NOTES					
14. ABSTRACT The University of Texas San Antonio (UTSA) including Southwest Research Institute is developing engine health monitoring (EHM) technology that compliments the ongoing and planned research within AFRL. The program consists of three distinct but related task areas that span EHM from a systems engineering level, to a specific damage-based life prediction processor, to a durability assessment of sensing materials. Task 1 is a systems level capstone effort focused on the information management, diagnostics and prognostics of EHM systems. The objectives are to develop Bayesian learning and neural networks for learning the unknown aspects of nonlinear engine systems and sensor sensitivity analysis. Task 2 is focused on developing a probabilistic fracture mechanics model and ASIC (application specific integrated circuit) implementation for efficient on-board and real-time assessment of the damage state of critical engine components. The effort is to develop hardware such that sophisticated probabilistic fracture mechanics algorithms can be placed on-board for evaluation of detected defects. Task 3 is focused on the development of much-needed durability models for thin film sensors that are either in common use or likely candidates for monitoring changes in engine performance or detecting and monitoring defects in fracture critical engine components.					
15. SUBJECT TERMS					
16. SECURITY CLASSIFICATION OF: Unclassified			17. LIMITATION OF ABSTRACT  unlimited	18. NUMBER OF PAGES  64	19a. NAME OF RESPONSIBLE PERSON C. L. Philip Chen
a. REPORT	b. ABSTRACT	c. THIS PAGE			19b. TELEPHONE NUMBER (include area code) 210-458-7076

AFRL-SR-AR-TR-07-0062

## **Final Report**

# **INNOVATIVE METHODS FOR ENGINE HEALTH MONITORING**

## **AFOSR Grant FA9550-04-1-0254**

**Drs. Philip Chen<sup>1</sup>, Z. Pantic-Tanner<sup>2</sup>, H. Millwater<sup>3</sup>, S. Hudak<sup>4</sup>, Y. Huang<sup>5</sup>, P.  
Cotae<sup>6</sup>, D. Tanner<sup>7</sup>, E. John<sup>8</sup>, K.Chan<sup>9</sup>, X. Wang<sup>10</sup>**

- 1 – Professor and Chair, Electrical and Computer Engineering, College of Engineering (UTSA), 210-458-7076, 210-458-5947, pchen@utsa.edu**
- 2 – Former Dean, College of Engineering, University of Texas at San Antonio (UTSA), 210-458-4492, 210-458-5556, zptanner@utsa.edu**
- 3 – Assistant Professor Mechanical Engineering (UTSA), 210-458-4481, 210-458-6504, hmillwater@utsa.edu**
- 4 – Institute Scientist, Southwest Research Institute, 210-522-2330, 210-522-6965, shudak@swri.org**
- 5 – Assistant Professor, Electrical Engineering (UTSA), 210-458-6250, 210-458-5947, yhuang@utsa.edu**
- 6 – Assistant Professor, Electrical Engineering (UTSA), 210-458-6269, 210-458-5947, pcotae@utsa.edu**
- 7 – Research Professor, Electrical Engineering (UTSA), 210-458-6321, 210-458-6311, dtanner@utsa.edu**
- 8 – Associate Professor, Electrical Engineering (UTSA), 210-458-5590, 210-458-5947, ejohn@utsa.edu**
- 9 – Institute Scientist, Southwest Research Institute, 210-522-2053, 210-458-6965, kchan@swri.org**
- 10 – Associate Professor, Mechanical Engineering (UTSA), 210-458-5565, 210-458-6504, xwang@utsa.edu**

**The University of Texas at San Antonio, College of Engineering  
6900 N. Loop 1604 W  
San Antonio, TX 78249**

**DISTRIBUTION STATEMENT A**  
Approved for Public Release  
Distribution Unlimited



## Table of Contents

Abstract.....	1
Project Summary .....	1
T1.1 Background & Objectives .....	1
T1.2 Approach and Accomplishments.....	2
T2.1 Background & Objectives .....	3
T2.2 Approach and Accomplishments.....	3
T3.1 Background & Objectives .....	4
T3.2 Approach and Accomplishments.....	5
Introduction.....	7
1. Engine, Sensor and Data Communication Systems Modeling.....	7
1.1 Background and Objectives .....	7
1.2 First Quarter Accomplishment.....	7
1.3 Second Quarter Accomplishment .....	8
1.4 Third Quarter Accomplishment .....	8
1.5 Final Accomplishment.....	8
1.5.1 On-line Sensor Validation with Expectation Propagation (EP) .....	8
1.5.2 Sensor Validation of a Planetary Rover system with EP...10	
1.5.3 Bluetooth Piconets in the Presence of Mutual Interference.....	12
2. Development of a Probabilistic Fracture Mechanics Model for Implementation in an Application Specific Integrated Circuit .....	15
2.1 Background & Objectives .....	15
2.2 Data Filtering Process .....	18
2.2.1 Procedure .....	18
2.2.2 Example .....	18
2.3 Rainflow Cycle Counting (Range-Pair Method) .....	21
2.3.1 Cycle-Extraction Method .....	21

2.3.2 Verification .....	21
2.4 Fatigue Analysis .....	24
2.4.1 Paris Law .....	24
2.4.2 Verification .....	25
2.4.2.1 Constant Amplitude Loading .....	25
2.4.2.2 Variable-Amplitude Loading (real engine data: Air to Ground).....	28
2.4.2.3 Various Mission Types.....	31
2.5 Monte Carlo Simulation.....	36
2.5.1 Histogram.....	36
2.5.2 Kernel Density Distribution .....	39
2.5.3 Test for Bayesian Updating .....	41
2.5.3.1 Test a Bayesian using a Textbook Sample .....	41
2.5.3.2 Test a Bayesian using a Real Engine Data.....	43
2.6 On Board Testing for Real Time Demonstration.....	44
2.6.1 Methods.....	45
2.6.2 Real Time Animation Using Code Composer Studio.....	45
2.6.3 Sample Rate Performance Analysis.....	48
3. DURABILITY OF SENSING MATERIALS .....	49
3.1 Background & Objectives.....	49
3.2 First Quarter Accomplishment.....	50
3.3 Second Quarter Accomplishment.....	51
3.4 Third Quarter Accomplishment.....	54
3.5 Final Accomplishment.....	54
3.5.1 Interface Fracture in FeCo/Ti-6Al-4V.....	55
3.5.2 Debonding Stress for FeCo/Ti-6Al-4V.....	58
3.5.3 Fracture Mechanisms.....	60
3.5.4 Fatigue Life Response.....	62
3.5.5 Conclusions .....	63



## **ABSTRACT**

The University of Texas San Antonio (UTSA) is developing engine health monitoring (EHM) technology that compliments the ongoing and planned research within AFRL. The UTSA team, which also includes Southwest Research Institute, is focusing on key technology areas including engine probabilistic-based diagnostics and prognostics, probabilistic life prediction, and the materials science aspects of sensors.

The program consists of three distinct but related task areas that span EHM from a systems engineering level, to a specific damage-based life prediction processor, to a durability assessment of sensing materials. Task 1 is a systems level capstone effort focused on the information management, diagnostics and prognostics of EHM systems. The objectives are to develop Bayesian learning and neural networks for learning the unknown aspects of nonlinear engine systems and sensor sensitivity analysis. Task 2 is focused on developing a probabilistic fracture mechanics model and ASIC (application specific integrated circuit) implementation for efficient on-board and real-time assessment of the damage state of critical engine components. The effort is to develop hardware such that sophisticated probabilistic fracture mechanics algorithms can be placed on-board for evaluation of detected defects. Task 3 is focused on the development of much-needed durability models for thin film sensors that are either in common use or likely candidates for monitoring changes in engine performance or detecting and monitoring defects in fracture critical engine components.

## **Project Summary**

### ***Task 1. Engine, Sensor & Data Communication Systems Modeling***

#### **T1.1 Background & Objectives**

Recent interest in unmanned aircraft and vehicles has increased the need to accommodate failures of its components such as actuators and sensors within the control systems. Since faulty sensor readings can lead to undesirable situations such as dispatch delays, degraded engine performance, and possibly unsafe operation, sensor validation is an essential task in the safe operation of an aircraft engine. A sensor fault is a deviation from the sensor's expected behavior. Experience has shown that even carefully designed and tested sensors may encounter such faults. Consequently, timely detection and validation of sensor faults are very important for safe and efficient engine operations.

To mitigate the risk associated with engine sensor faults, we have proposed a model-based probabilistic sensor model that is able to identify sensor faults and to correct them where there is redundancy in the sensor information. Our current objectives include designing a model-based sensor validation model and engine modeling, and development of a detection mechanism that is to discover the occurrences of sensor faults. Since more advanced wireless technology capable of operating in the high temperature engine environment is not available at this moment, as the preparation for the future work, we have studied Bluetooth wireless technology as the framework in this research. With the given information from multiple remote sensors that needs to be processed, the Bluetooth technology is investigated in order to assess the real performance and coexistence issues of wireless sensors in the presence of mutual

interference. Analytical lower bounds on the aggregated throughput offered by Bluetooth technology are evaluated at the optimal operating conditions.

## T1.2 Approach and Accomplishments

We have studied and designed simulation models that have included probabilistic information of sensors. Since faulty sensor readings can lead to an unreliable situation, such as dispatch delays and possible unsafe operation, fast and accurate sensor validation is a crucial component for guaranteed system performance. Built-in-test (BIT) is an approach becoming popular in many new complex systems and can likely be extended to include sensors. Along these lines, we describe a Markov-jump state space model approach. We also construct a neural network engine simulation model to “learn or capture” the unknown aspects that occur in a more traditional nonlinear state-space model. We develop several Bayesian solutions to sensor validation, based on particle filtering algorithms: Mixture Kalman filter and Stochastic-M algorithms, and expectation maximization (EP) algorithm. In general, the EP algorithm has less complexity and better accuracy. The block diagram of the designed system is shown in Figure 1.

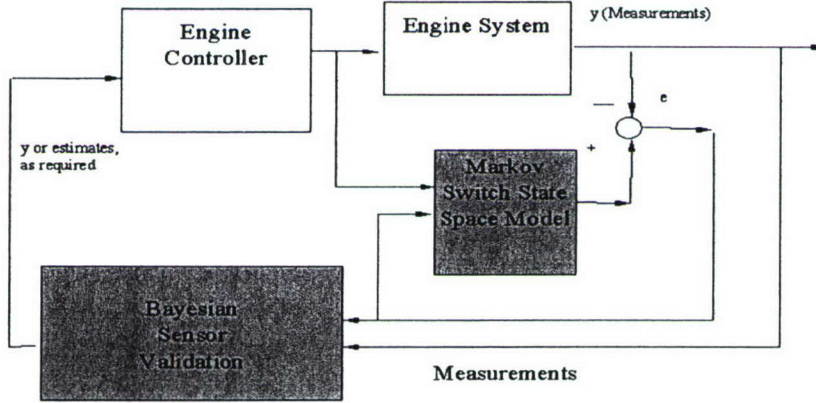


**Figure 1: Block diagram of the designed system**

As for the progress of wireless sensor technology, we have explored actual state of art of sensor technology (hardware and technical literature) for monitoring an aircraft engine, and focused on a model for the wireless architecture for short-range data communications. In addition, we derived a completely analytical framework, which allows the determination of the aggregate throughput offered by a group of co-located Piconets, as well as the determination of the optimal operating conditions while taking propagation aspects into account. For data communication, we also explore the performance of several Piconets located in the same region that follows an IEEE802.11b standard. An approximated threshold-based approach on Bluetooth Piconets is proposed to determine the probability of packet collision. Assuming interference limited operating conditions caused by the presence of the interference due to the packet losses, we have developed result of receiving maximum throughput given randomly distributed sensor coverage areas.



## ***Task 2. Development of a Probabilistic Fracture Mechanics Model for Implementation in an Application Specific Integrated Circuit***

### **T2.1 Background & Objectives**

The current state-of-the-art in engine health monitoring (EHM) is focused on detecting vibration signals, oil debris, foreign object damage, and other engine health indicators, interpreting the signals and making diagnostic and prognostics decisions. Sometimes a wear model is included to estimate remaining life. EHM technology at this point in time attempts to sense the presence of a crack through indirect measurements such as vibration abnormalities. Some success is reported in spin pit testing but application in an on-board setting is dubious.

There has been a tremendous advance in the science and computational ability to predict the behavior of cracks (size, cycles to failure) in the past 50 years. There are now several sophisticated computer codes for crack propagation calculations such as DARWIN®, NASGRO®, and AFGROW. These codes have many man-years of investment in algorithm development, materials characterization and code verification. However, at best these codes can be used in a design mode or an after the fact analysis given a download of the data from an engine. Currently, trained neural networks are used to implement a mechanical or material degradation in order to get real-time performance. However, neural networks must be trained for each particular situation and cannot model the capabilities in today's and tomorrow's fracture mechanics codes.

In order to get real-time performance and use the sophisticated fracture mechanics knowledge, we will implement a probabilistic fracture mechanics algorithm in hardware to facilitate real-time estimation of crack behavior and structural integrity. The objective of this research is to develop and test an ASIC (Application Specific Integrated Circuit) that implements a probabilistic fracture mechanics algorithm for real-time assessment of structural integrity of engine components. The initial focus will be on gas turbine engine disks, however this technology is pervasive and therefore could be extended to other engine components, as well as other structural systems, e.g., airframes, off-shore structures.

The algorithm, implemented in hardware, will provide a real-time probability of fracture estimate for the engine component (initial focus is the disk) given loading inputs, material properties, initial crack size estimate and other inputs, see technical details below, using low-cycle fatigue (LCF) crack propagation fracture mechanics.

### **T2.2 Approach and Accomplishments**

A Matlab program was initiated for prototyping the computational algorithms with the initial focus being the development of a rainflow algorithm for determining and extracting damaging fatigue stress cycles in a real-time setting. The rainflow and crack growth algorithms were combined and used to simulate crack growth as a function of engine usage, and the crack growth computed was compared against results from well-established fatigue programs DARWIN® and AFGROW. Subsequently, a probabilistic crack growth algorithm has been implemented by incorporating a Monte Carlo algorithm to consider uncertainties in localized stresses and crack growth rates.

On-board implementation has focused on the implementation of the deterministic low cycle fatigue algorithm on a TI DSP Processor. The processing board and sample results are shown in the figure below, see Figures 2 and 3. The input signal represents the engine component RPM values during a representative flight are shown in Figure 3a. The values are converted into localized stress levels by the on-board algorithm, damaging stress pairs are determined, and crack growth is computed. The cumulative crack growth is shown in Figure 3b.

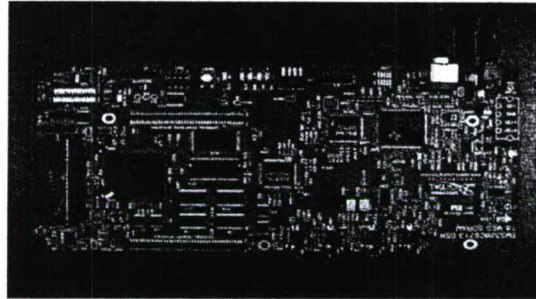


**Figure 2: Processing Board**

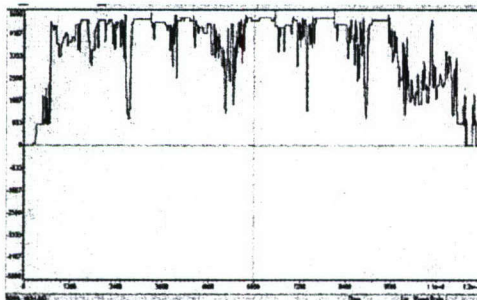


**Figure 3a. Input Signal**

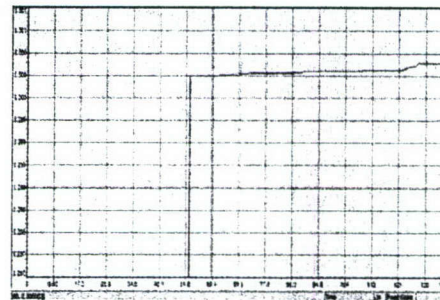


**Figure 3b. Crack Growth**

### ***Task 3. DURABILITY OF SENSING MATERIALS***

#### **T3.1 Background & Objectives**

Vehicle health management (VHM) requires on-board sensors that are typically actuated using materials that exhibit shape memory, piezoelectric, or magnetostrictive behavior. In many cases, these sensing materials are used in the form of multi-layered structures whose functionalities and performance characteristics are intimately linked to their nanocrystalline or amorphous states. Furthermore, the durability and functionalities of thin-film materials are known to depend on layer thickness and likely on test temperature. Unfortunately, these material properties are generally not available for thin-film materials. Since on-board sensing devices must be more durable than the components that are being monitored, there is a strong need determine the operative damage mechanism and to characterize the durability of thin-film sensing materials in the pertinent size scale and under conditions that are relevant to the service environment, which usually involves fatigue or thermomechanical loading. The initial focus of this effort will be on magnetostrictive thin film sensor materials because of the anticipated importance to VHM and relative lack of durability information.



The objectives of this task are: (1) to determine the durability of magnetostrictive sensing materials subjected to mechanical, electrical, and thermal loading, (2) to evaluate the dependence of the performance and durability on layer thickness, and service temperature, and (3) to develop a durability model to optimize sensor durability with respect to layer thickness and interfacial strength. The first year of this program has focused on a room temperature assessment, while elevated temperature assessments are planned for years two and three.

### **T3.2 Approach and Accomplishments**

An integrated experimental/nanomechanical modeling approach is being utilized to achieve the task objectives. Innovative processing techniques are being used to deposit thin-film sensor materials on an engineering alloy substrate. Novel experimental techniques are being employed to characterize the microstructure, yield strength, fatigue, and sensing (i.e., magnetostrictive) properties of the thin-film sensor materials at ambient temperature. The effects of layer thickness, temperature, and interfacial strength on the mechanical and functional properties are being interrogated and correlated to the underlying nanocrystalline state in order to identify the pertinent failure mechanisms. This fundamental understanding is being used to model the failure process at the nanoscale level. The initial low temperature results are applicable to fan applications (including the critical JSF lift fan), whereas the elevated temperature results proposed in the later years of the program would be applicable to fracture critical compressor and turbine components.

The results indicated that the interface toughness of FeCo/Ti-6Al-4V measured by an indentation technique is independent of layer thickness at ambient temperature. The critical stress for interface debonding increased with decreasing layer thickness according to a critical energy release rate criterion. Ion-cleaning improves adhesion, enhance the interface toughness and increase the debonding stress of the thin films, as illustrated in Figure 4. The resulting interface is relatively weak thereby preventing crack penetration into Ti-6Al-4V substrate – thus interfacial strength can be engineered to prevent damage to the substrate. As a result, the FeCo thin films did not alter the fatigue life of the Ti-6Al-4V substrate. The presence of microcracks and localized interface debonds in the thin films did not affect the functionality of the sensor to detect strain via the inverse magneto-elastic effect. The overall durability of the films was optimized to be in the range needed for practical application of the film as an imbedded sensor.

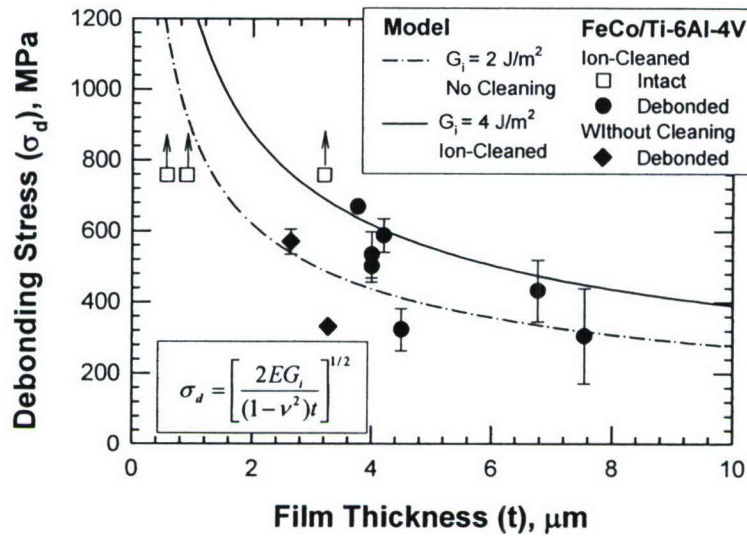


**Figure 4.** Ion-cleaning increased the interface toughness from  $2 \text{ J/m}^2$  to  $4 \text{ J/m}^2$  and increased the debonding stress to provide a durable FeCo thin film. A comparison of the measured and predicted debonding stresses for FeCo thin films on Ti-6Al-4V shows that the debonding stress in FeCo thin film increases with decreasing film thickness according to a critical elastic energy release rate criterion shown in the inserted equation.

Accomplishments of this task include (1) measuring the elastic and hardness properties of FeCo thin films by nanoindentation, (2) characterizing the interface properties and identifying the fracture mechanisms in FeCo/Ti-6Al-4V, (3) optimizing the processing condition and the interface properties to achieve a durable FeCo thin film that did not cause a fatigue life debit to the Ti-6Al-4V substrate, (4) a demonstration of the functionality of the FeCo thin films as a strain and crack detection sensor in the presence of micorcracks and interface debonds, and (5) the formulation of a strategy for optimizing interfacial strength so that thin films can be engineered to meet the durability requirement for embedded sensors without damaging the substrate.

We have discovered that interface toughness of FeCo/Ti-6Al-4V is independent of layer thickness and found out that delamination strength of FeCo/Ti-6Al-4V increases with decreasing layer thickness. Also, we found out that weak interface prevents crack penetration into Ti-6Al-4V substrate – thus interfacial strength can be engineered to prevent damage to the substrate. We have discovered that low-cycle fatigue lives of Ti-6Al-4V are identical with and without FeCo thin films. Our major achievement is that we are able to identified strategy of optimizing interfacial strength so that thin films can be engineered to meet the durability requirement for embedded sensors



## **Introduction**

The UTSA Engine Health Monitoring project covers three major task areas which are described here as: (1) System modeling of engine and sensor systems using neural networks and Bayesian learning. Data communication is also an aspect of the modeling. (2) Development of a probabilistic fracture mechanics model and a design for a hardware implementation. (3) The durability and development of sensor materials. For convenience this report is organized under these three areas and each task area includes a background & objectives description, a progress description for each quarter, and references in each area.

## **1. Engine, Sensor & Data Communication Systems Modeling**

### **1.1 Background & Objectives**

Recent interest in unmanned aircraft and vehicles has increased the need to accommodate failures of its components such as actuators and sensors within the control systems. Since faulty sensor readings can lead to undesirable situations such as dispatch delays, degraded engine performance, and possibly unsafe operation, sensor validation is an essential task in the safe operation of an aircraft engine. A sensor fault is a deviation from the sensor's expected behavior. Experience has shown that even carefully designed and tested sensors may encounter such faults. Consequently, timely detection and validation of sensor faults are very important for safe and efficient engine operations.

To mitigate the risk associated with engine sensor faults, we have proposed a model-based probabilistic sensor model that is able to identify sensor faults and to correct them where there is redundancy in the sensor information. Our current objectives include designing a model-based sensor validation model and engine modeling, and development of a detection mechanism that is to discover the occurrences of sensor faults. With the given information from multiple remote sensors that needs to be processed, the Bluetooth technology is investigated in order to assess the real performance and coexistence issues of wireless sensors in the presence of mutual interference. Analytical lower bounds on the aggregated throughput offered by Bluetooth technology are evaluated at the optimal operating conditions.

### **1.2 First Quarter Accomplishment**

We have investigated both linear and non-linear principal component analysis (PCA) of sensor information in the first quarter. We also studied and designed simulation models that have included probabilistic information of sensors. As for the progress of wireless sensor technology, we have explored actual state of art of sensor technology (hardware and technical literature) for monitoring an aircraft engine, and focused on a model for the wireless architecture for short-range data communications. We also

studied the software package of the Bluetooth system in order to be coupled with a low speed data acquisition/host processor board.

### 1.3 Second Quarter Accomplishment

We have investigated in this quarter the design of a sensor validation model for detection of the occurrence of a sensor fault, i.e., fault detection and identification of fault type, i.e., fault identification. We also selected possible inference algorithms that could be used for the validation model. In addition, we derived a completely analytical framework, which allows the determination of the aggregate throughput offered by a group of co-located Piconets, as well as the determination of the optimal operating conditions while taking propagation aspects into account.

### 1.4 Third Quarter Accomplishment

We have investigated the problem of on-line sensor validation. Since faulty sensor readings can lead to an unreliable situation, such as dispatch delays and possible unsafe operation, fast and accurate sensor validation is a crucial component for guaranteed system performance. Built-in-test (BIT) is an approach becoming popular in many new complex systems and can likely be extended to include sensors. Along these lines we describe a Markov-jump state space model approach. We also construct a neural network engine simulation model to “learn or capture” the unknown aspects that occur in a more traditional nonlinear state-space model. For data communication, we also explore the performance of several Bluetooth Piconets located in the same region that follows an IEEE802.11b standard. An approximated threshold-based approach on Bluetooth Piconets is proposed to determine the probability of packet collision.

### 1.5 Final Accomplishment

We have developed an alternative Bayesian solution to sensor validation based on expectation maximization (EP) algorithm. This method can on-line track sensor state efficiently. We investigate the application of the developed EP algorithm to a realistic system of a planetary rover of Mars. The results show that compared with Mixture Kalman Filter developed in the third quarter, the EP has less complexity and better accuracy.

#### 1.5.1 On-line Sensor Validation with Expectation Propagation (EP)

We lay out in this section the steps of EP algorithm for sensor validation on the hybrid DSSM (1). For easy composition, we first explain the notations in the algorithm of EP:  $q(\mathbf{x}_t | \mathbf{y}_{1:t-1}) = \mathcal{N}(\mathbf{x}_t | \hat{\mathbf{x}}_{t|t-1}, \mathbf{P}_{t|t-1})$  is the predictive density of  $\mathbf{x}_t$ ;

$q(\mathbf{x}_t | \mathbf{y}_{1:t}) = \mathcal{N}(\mathbf{x}_t | \hat{\mathbf{x}}_{t|t}, \mathbf{P}_{t|t})$  is the posterior of  $\mathbf{x}_t$ ;

$q(\mathbf{x}_t | \mathbf{y}_{1:T}, -t) = \mathcal{N}(\mathbf{x}_t | \hat{\mathbf{x}}_{-t|T}, \mathbf{P}_{-t|T})$

is the smoothing density of  $\mathbf{x}_t$  without the current observation  $\mathbf{y}_t$ ;  $q(\mathbf{y}_t | \mathbf{x}_t) = \mathcal{N}(\hat{\mu}_t, \hat{\lambda}_t)$

is the likelihood of  $\mathbf{y}_t$  given  $\mathbf{x}_t$ ;  $q(s_t | \mathbf{y}_{1:t-1}) = \text{Discrete}(q(s_t = 1 | \mathbf{y}_{1:t-1}), \dots, q(s_t = M | \mathbf{y}_{1:t-1}))$  is the filtering prior of  $s_t$ ;  $q(s_t | \mathbf{y}_{1:T}, -t) = \text{Discrete}(q(s_t = 1 | \mathbf{y}_{1:T}, -t), \dots, q(s_t = M | \mathbf{y}_{1:T}, -t))$  is the smoothing prior of  $s_t$ ;  $q(s_t | \mathbf{y}_{1:t}) = \text{Discrete}(q(s_t = 1 | \mathbf{y}_{1:t}), \dots, q(s_t = M | \mathbf{y}_{1:t}))$



$y_{1:t})$  is the posterior of  $s_t$ .  $Z = \sum_{s_t} q(s_t|y_{1:t-1}) \mathcal{N}(\mathbf{H}_{s_t} \hat{\mathbf{x}}_{t|t-1}, \mathbf{H}_{s_t} \mathbf{P}_{t|t-1} \mathbf{H}_{s_t}^\top + \mathbf{C}_v)$  is the normalizing constant;  $\mathbf{K}_t$  is the Kalman gain and  $\mathbf{J}_t$  is the smoothing gain. The algorithm of EP for sensor validation can be summarized in the following:

For current = 1 : T

- 1. Initial estimate
  - Obtain the predictive density

$$\begin{aligned}\hat{\mathbf{x}}_{t|t-1} &= \mathbf{F} \hat{\mathbf{x}}_{t-1|t-1} + \mathbf{G} \mathbf{U} \\ \mathbf{P}_{t|t-1} &= \mathbf{F} \mathbf{P}_{t-1|t-1} \mathbf{F}^\top + \mathbf{C}_w \\ q(s_t|y_{1:t-1}) &= \sum_{s_{t-1}} \mathbf{P}_{t|s_{t-1}, s_t} q(s_{t-1}|y_{1:t-1})\end{aligned}$$

- Moment matching

$$\begin{aligned}r_{t,i} &= \frac{q(s_t=i|y_{1:t-1}) \mathcal{N}(y_t|\mathbf{H}_i \hat{\mathbf{x}}_{t|t-1}, \mathbf{P}_{y_t})}{Z} \\ \hat{\mathbf{x}}_{t|t} &= \frac{\sum_{s_t \in \mathcal{A}} q(s_t|y_{1:t-1}) \mathcal{N}(y_t|\hat{\mathbf{y}}_t, \mathbf{P}_{y_t}) \hat{\mathbf{x}}'_{t|t}}{Z} \\ \mathbf{P}_{t|t} &= \frac{\sum_{s_t \in \mathcal{A}} q(s_t|y_{1:t-1}) \mathcal{N}(y_t|\hat{\mathbf{y}}_t, \mathbf{P}_{y_t}) (\hat{\mathbf{x}}'_{t|t} \hat{\mathbf{x}}'^{\top}_{t|t} + \mathbf{P}'_{t|t})}{Z} \\ &\quad - \hat{\mathbf{x}}_{t|t} \hat{\mathbf{x}}_{t|t}^\top\end{aligned}$$

where

$$\begin{aligned}\hat{\mathbf{x}}'_{t|t} &= \hat{\mathbf{x}}_{t|t-1} + \mathbf{K}_t (y_t - \mathbf{H}_{s_t} \hat{\mathbf{x}}_{t|t-1}) \\ \mathbf{P}'_{t|t} &= (\mathbf{I} - \mathbf{K}_t \mathbf{H}_{s_t}) \mathbf{P}_{t|t-1} \\ \mathbf{K}_t &= \mathbf{P}_{t|t-1} \mathbf{H}_{s_t}^\top (\mathbf{H}_{s_t} \mathbf{P}_{t|t-1} \mathbf{H}_{s_t}^\top + \mathbf{C}_v)^{-1}\end{aligned}$$

- Obtain the estimated likelihood

$$\begin{aligned}\mu_t &= \hat{\lambda}_t^{-1} \hat{\mu}_t \\ &= (\mathbf{P}_{t|t})^{-1} \hat{\mathbf{x}}_{t|t} - (\mathbf{P}_{t|t-1})^{-1} \hat{\mathbf{x}}_{t|t-1} \\ \lambda_t &= \hat{\lambda}_t^{-1} = (\mathbf{P}_{t|t})^{-1} - (\mathbf{P}_{t|t-1})^{-1} \\ q(y_t|s_t=i) &= q(s_t=i|y_{1:t})/q(s_t=i|y_{1:t-1})\end{aligned}$$

- 2. Loop until the maximum number of iteration is reached or convergence happens.

- For t = current : -1 : current-window-size+1
  - Kalman smoothing when  $t < \text{current}$

$$\begin{aligned}\mathbf{J}_t &= \mathbf{P}_{t|t} \mathbf{F}^\top \mathbf{P}_{t+1|t}^{-1} \\ \hat{\mathbf{x}}_{t|T} &= \hat{\mathbf{x}}_{t|t} + \mathbf{J}_t (\hat{\mathbf{x}}_{t+1|T} - \mathbf{F} \hat{\mathbf{x}}_{t|t}) \\ \mathbf{P}_{t|T} &= \mathbf{P}_{t|t} + \mathbf{J}_t (\mathbf{P}_{t+1|T} - \mathbf{P}_{t+1|t}) \mathbf{J}_t^\top\end{aligned}$$

- Delete old likelihood

$$\begin{aligned}\mathbf{P}_{-t|T} &= (\mathbf{P}_{t|T}^{-1} - \lambda_t)^{-1} \\ \hat{\mathbf{x}}_{-t|T} &= \mathbf{P}_{-t|T} (\mathbf{P}_{t|T}^{-1} \hat{\mathbf{x}}_{t|T} - \mu_t) \\ q(s_t=i|y_{1:T,-t}) &= \frac{q(s_t=i|y_{1:t})}{q(y_t|s_t=i)}\end{aligned}$$

- Incorporate the likelihood and moment matching

$$\begin{aligned}q(s_t=i|y_{1:t}) &= \frac{q(s_t=i|y_{1:T,-t}) \mathcal{N}(y_t|\mathbf{H}_i \hat{\mathbf{x}}_{-t|T}, \mathbf{P}_{y_t})}{Z} \\ \hat{\mathbf{x}}_{t|t} &= \frac{\sum_{s_t \in \mathcal{A}} q(s_t|y_{1:T,-t}) \mathcal{N}(y_t|\hat{\mathbf{y}}_t, \mathbf{P}_{y_t}) \hat{\mathbf{x}}''_{t|t}}{Z} \\ \mathbf{P}_{t|t} &= \frac{\sum_{s_t \in \mathcal{A}} q(s_t|y_{1:T,-t}) \mathcal{N}(y_t|\hat{\mathbf{y}}_t, \mathbf{P}_{y_t}) (\hat{\mathbf{x}}''_{t|t} \hat{\mathbf{x}}''^{\top}_{t|t} + \mathbf{P}''_{t|t})}{Z} \\ &\quad - \hat{\mathbf{x}}_{t|t} \hat{\mathbf{x}}_{t|t}^\top\end{aligned}$$

where

$$\begin{aligned}\hat{\mathbf{x}}_{t|t}'' &= \hat{\mathbf{x}}_{-t|T} + \mathbf{K}_t(\mathbf{y}_t - \mathbf{H}_{s_t}\hat{\mathbf{x}}_{-t|T}) \\ \mathbf{P}_{t|t}'' &= (\mathbf{I} - \mathbf{K}_t\mathbf{H}_{s_t})\mathbf{P}_{-t|T} \\ \mathbf{K}_t &= \mathbf{P}_{-t|T}\mathbf{H}_{s_t}^T(\mathbf{H}_{s_t}\mathbf{P}_{-t|T}\mathbf{H}_{s_t}^T + \mathbf{C}_v)^{-1}\end{aligned}$$

- Obtain new likelihood for the next refinement

$$\begin{aligned}\mu_t &= (\mathbf{P}_{t|t})^{-1}\hat{\mathbf{x}}_{t|t} - (\mathbf{P}_{-t|T})^{-1}\hat{\mathbf{x}}_{-t|T} \\ \lambda_t &= \hat{\lambda}_t^{-1} = (\mathbf{P}_{t|t})^{-1} - (\mathbf{P}_{-t|T})^{-1} \\ q(\mathbf{y}_t | s_t = i) &= \frac{q(s_t = i | \mathbf{y}_{1:t})}{q(s_t = i | \mathbf{y}_{1:T}, -t)}\end{aligned}$$

- For  $t = \text{current-window-size} + 1 : \text{current}$ 
  - Get the predictive densities, which are the same as (7)(8)(9)
  - Incorporate the true likelihoods into posterior distribution

$$\begin{aligned}\mathbf{P}_{t|t} &= (\mathbf{P}_{t|t-1}^{-1} + \lambda_t)^{-1} \\ \hat{\mathbf{x}}_{t|t} &= \mathbf{P}_{t|t}(\mu_t + \mathbf{P}_{t|t-1}^{-1}\hat{\mathbf{x}}_{t|t-1}) \\ q(s_t = i | \mathbf{y}_{1:t}) &= q(\mathbf{y}_t | s_t = i)q(s_t = i | \mathbf{y}_{1:T}, -t)\end{aligned}$$

### 1.5.2 Sensor Validation of a Planetary Rover system with EP

The developed EP is applied to a realistic system of a planetary rover of Mars. The model is a high dimensional hybrid state space model or called linear switching model. It consists of one continuous state  $\mathbf{x}_t$ , one discrete state  $s_t$  and an observation variable  $\mathbf{y}_t$ . The continuous state  $\mathbf{x}_t$  includes six system parameters that capture the dynamic evolution of the automaton, and the discrete state  $s_t$  represents 6 different fault states or operational modes of the system. The reason that we use this model is that it has more realistic meanings than other mathematical models for engine fault diagnosis. Particle filters, such as risk-sensitive PF, variable resolution PF, Rao-Blackwellized PF, have been mentioned [10] and used on this model [11]. Our purpose of using EP is to show the simplicity and comparable result of EP with Particle filters.

The model is described as follows

$$\begin{cases} p(s_t = m | s_{t-1} = n) = T(n, m) \\ \mathbf{x}_t = \mathbf{F}(s_t, s_{t-1})\mathbf{x}_{t-1} + \mathbf{u} + \mathbf{p}n_t \\ \mathbf{y}_t = \mathbf{H}\mathbf{x}_t + \mathbf{v}_t \end{cases}$$

where  $T(n, m)$  is transition matrix of the discrete state  $s_t$ ;  $\mathbf{F}(\cdot)$  denotes the state matrix, which depends on previous and current discrete states;  $\mathbf{H}$  is measurement matrix, which is independent of the discrete and continuous states;  $\mathbf{u}$  is the input;  $\mathbf{n}_t$  and  $\mathbf{v}_t$  are Gaussian noise vectors. The discrete state  $s_t$  has six modes that refer to flat driving, rock under front wheel, rock under middle wheel, rock under rear wheel, rock between front and middle wheel and rock between middle and rear wheel, respectively. The six parameters of the continuous state represent the rocker and bogey angles and their derivatives, rock width and rock height. Rocker-bogey is a



suspension system. The model is used to describe the response of the suspension system to driving over rocks and other obstacles to simulate situations where the rover's scientific instruments could collide with an obstacle, or where the rover could become "high-centered" on a rock. The only two outputs are the rocker and bogey angles. One difficulty of this model is how to describe the state matrix  $F(.,.)$ . It is hard to be expressed by a single matrix, since it is a series of nonlinear sequential reactions, involving the previous and current discrete states. We compare through computer simulation the performance of the EP with a particle filter, the mixture Kalman filter (MKF), developed in the 3<sup>rd</sup> quarter. In our experiment, we used 500 consecutive observations. We compared the performance in terms of accuracy and complexity. For EP, we defined the convergence as the KL distance between  $q(s_i)$ s from two consecutive EP iterations less than  $1e-3$ . Based on this criterion, our simulation indicated that, most of time, EP converges within 2 iterations. For MKF, 50 particles were used. In Figure 1.1, we plotted the number of fault detection errors vs. SNR and it clearly demonstrates the better performance of EP. Especially, when the noise is large, EP generates a lot less errors than the MKF. We also compare the complexity of the two algorithms. We considered the complexity in terms of the computer run-time of for 500 time steps and the simulation indicated that EP finished within 12.05s while MKF took 15.82s. It is evident that EP has less complexity than MKF.

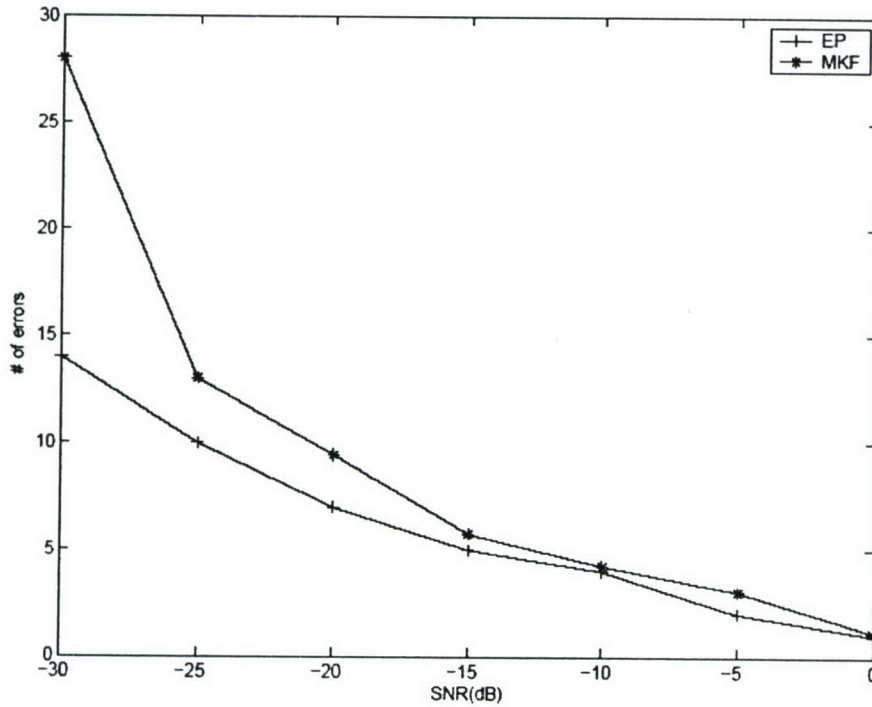


**Figure 1.1. Number of errors per 500 time steps at different SNRs**

### 1.5.3 Bluetooth Piconets in the Presence of Mutual Interference

In previous three phases of this project the coexistence issue has been investigated in the case of IEEE802.11b low-rate link (1 Mb/s) interfered by a set of Bluetooth piconets. We explored the possibility to introduce traffic shaping techniques, to reduce the effect of interference for data traffic types. The effect of fading was also taken into account by simplified assumptions where some performance measures, such as the packet error rate, the number of packet retransmissions and the transmission latency, were introduced.

The goal of this task is to investigate the analytical coexistence of Bluetooth piconets taking the interference issues into account in a more complicated setting and to provide analytical tools for performance evaluation. Generally speaking, to obtain the overall system performance, a bit level simulation combined with a protocol level simulation does not represent a practical solution due to prohibitive computational time required. Hence, there is the necessity to introduce new accurate and simple methods to performance evaluation that avoid simulation. Based on the previous analytical results in Q1-Q3 reports we assume that only a terminal can transmit at a time in a piconet, the number of  $\eta-1$  piconets surrounding the reference piconet coincide with the number of potentially interfering transmission.

We are interested in the average packet error probability experienced by the reference master which is given by

$$P_{ep} = 1 - (1 - P_{err})^{\eta-1} = \begin{cases} 1 - \left(1 - \frac{K^2 R_u^2}{2R^2} pr\right)^{\eta-1}, & \text{if } KR_u \leq R \\ 1 - \left[1 - \left(1 - \frac{K^2 R_u^2}{2R^2} pr\right)\right]^{\eta-1}, & \text{otherwise} \end{cases} \quad \text{Eq. 1.5.3a}$$

where:

- a)  $P_{err}$  is the probability of packet loss probability, derived in Q3 report,
- b)  $R_u$  is the maximum radius of a circular region of  $\eta$  unsynchronized piconets distributed uniformly in a circular region of radius  $R$ ,
- c)  $p$  is the probability of frequency collision, derived in Q2 report, and
- d) Interferer activity factor is denoted by  $r$  as in Q1 report.
- e)  $K$  is a properly protection radio factor.

The results are plotted in Figure 1.2.



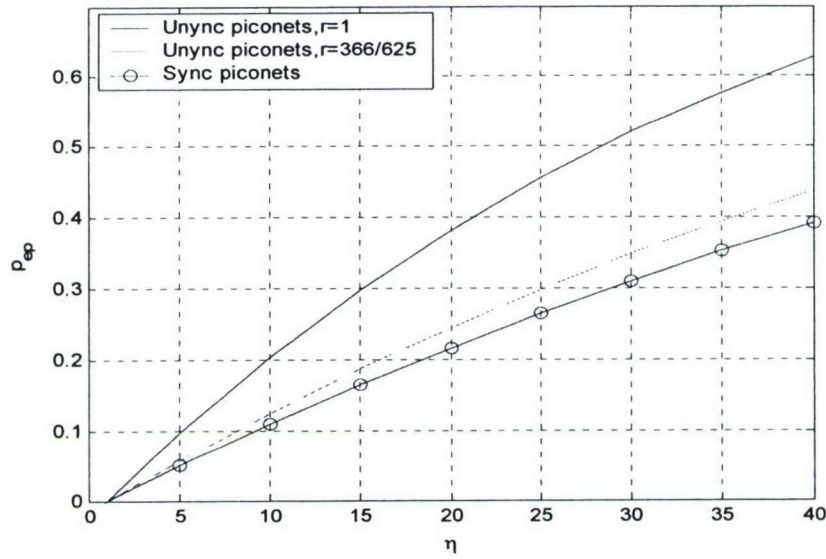


**Figure 1.2. Comparison between  $P_{ep}$  curves for  $\eta$  synchronized and unsynchronized piconets**

From the above figure we find out that if the piconets are synchronized then the probability of error is decreased. For practically issues and implementation of sensors we suggest using the synchronism of the transmission in order to diminish the mutual interference. The relation in Eq. 1.5.3a gives analytical relation so we don't need to do any simulation.

We are also interested in the optimization of the communication performance of the sensors in the context of information theory. This is quantized by the throughput bounds  $S_{bound}$  given below in two cases when  $KR_u \leq R$ , ( $D$  represents the length of the adopted packet type) DM1 or DH1, since we are considering one-slot transmission).

$$S_{bound} = \frac{\eta D}{T} \left( 1 - \frac{K^2 R_u^2}{2R^2} pr \right)^{\eta-1} \quad \text{Eq. 1.5.3b}$$

and when  $KR_u > R$

$$S_{bound} = \frac{\eta D}{T} \left[ 1 - \left( 1 - \frac{K^2 R_u^2}{2R^2} pr \right) \right]^{\eta-1} \quad \text{Eq. 1.5.3c}$$

In order to compare our results with the results predicted by information theory we need to plot these above results in the limiting regime i.e  $R/R_U = m$ ,  $m = 1, 2, 3$ .

The results are plotted in Figure 1.3.

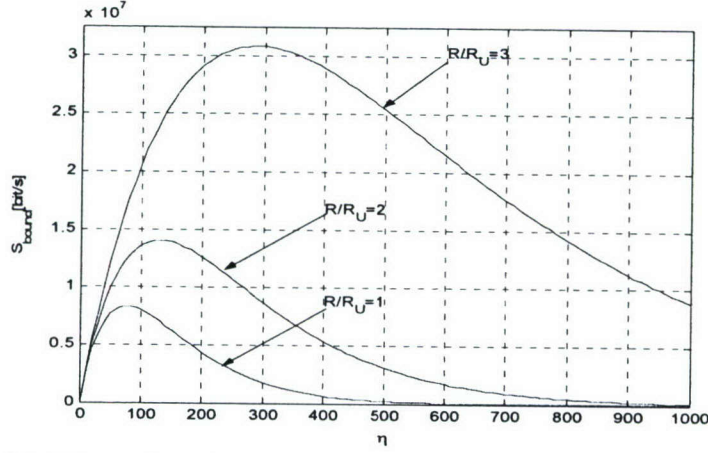


**Figure 1.3. Throughput in bits/sec of  $\eta$  piconets in the limiting regime and considering mutual interference**

The above figure is very important since it tells us how many sensors we can arrange or we can randomly distribute in a given area in order to get the maximum of the throughput. We assumed interference limited operating conditions caused by the presence of the interference due to the packet losses. Including other effects as exact position, the maximum communication rate for each sensor, sum capacity, information rate capacity, user sensors capacity, the best receiver for the master are open problems and are left for future research.

It is of interest to calculate the exact the number of sensor which maximize the above throughputs. The results are given below, for the  $KR_u \leq R$

$$\eta_{optim} = \frac{1}{\ln \left( \frac{1}{1 - \frac{K^2 R_u^2}{2R^2} pr} \right)} \quad \text{Eq. 1.5.3d}$$

and when  $KR_u > R$

$$\eta_{optim} = \frac{1}{\ln \left( \frac{1}{1 - \left( 1 - \frac{R^2}{2K^2 R_u^2} pr \right)} \right)} \quad \text{Eq. 1.5.3e}$$

### **Future Research**

Our models and analytical results developed in this task and overall in this research can be expanded further for specifically conditions, which take all the transmission aspects into account such as

- Propagation effects
- Interference
- Modulation format
- Coding techniques



And medium access control aspects

- Frequency hopping
- Packet structure
- Traffic load

## Reference

- [1] Y. M. Zhang and X. R. Li, "Detection and diagnosis of sensor and actuator failures using IMM estimator," *IEEE Transaction on Aerospace and Electronic Systems*, vol. 34, no. 4, pp. 1293–1313, Oct 1998.
- [2] Y. Bar-Shalom and X. R. Li, *Multitarget-Multisensor Tracking: Principle and Techniques*. Storrs, CT: YBS Publishing, 1995.
- [3] R. Chen and J. Liu, "Mixture Kalman filters," *Journal of Royal Statist. Soc. B*, vol. 62, pp. 493–508, 2000.
- [4] Y. Huang, J. Zhang, and P. M. Djurić, "Bayesian detection for BLAST," *IEEE Transactions on Signal Processing*, March 2005.
- [5] P. Fearnhead, "Sequential Monte Carlo method in filter theory," Ph.D. dissertation, Oxford University, England, 1998.
- [6] T. P. Minka, "A family of algorithms for approximate Bayesian inference," Ph.D. dissertation, MIT, Jan 2001.
- [7] T. Wei, Y. Huang, and Y. Qi, "Symbol detection with time-varying unknown phase by expectation propagation," in *To appear in ICASSP2005*, Philadelphia, PA, March 2005.
- [8] T. Guo and P. Chen, "Sensor Based Engine Life Calculation – A Probabilistic Perspectives," *ISABE*, 2003.
- [9] T. Guo, D. Mattern, L. Jaw, and P. Chen, "Model-Based Sensor Validation for a Turbofan Engine Using Auto-Associative Neural Networks," *Smart Engineering System Design*, 5:21-32, 2003.
- [10] Richard Dearden, Frank Hutter, Reid Simmons, Sebastian Thrun, Vandt Verma, and Thomas Willeke, Real-time Fault Detection and Situational Awareness for Rovers: Report on the Mars Technology Program Task. *Proceedings of IEEE Aerospace Conference*, March 2004.
- [11] Vandt Verma, Geoff Gordon, Reid Simmons, and Sebastian Thrun, "Particle Filters for Rover Fault Diagnosis," *IEEE Robotics & Automation Magazine* special issue on Human Centered Robotics and Dependability, June 2004

## **2. Development of a Probabilistic Fracture Mechanics Model for Implementation in an Application Specific Integrated Circuit**

### **2.1 Background & Objectives**

The current state-of-the-art in engine health monitoring (EHM) is focused on detecting vibration signals, oil debris, foreign object damage, and other engine health indicators, interpreting the signals and making diagnostic and prognostics decisions. Sometimes a wear model is included to estimate remaining life.

EHM technology at this point in time attempts to sense the presence of a crack through indirect measurements such as vibration abnormalities. Some success is reported in spin pit testing but application in an on-board setting is dubious.

Other research however is moving towards direct interrogation of the component material to sense damage that could pose a threat. For example, a new DARPA initiative on Material Prognosis is planning to address the detection of fatigue damage or cracking on a turbine disk by depositing a thin-film magnetostrictive material on the disk, exciting the sensor, creating a mechanical elastic wave in the disk, and recording the wave reflections. Processing of the reflected waves can indicate the presence of a crack. If a defect is detected, algorithms are needed to assess the severity of the defect.

There has been a tremendous advance in the science and computational ability to predict the behavior of cracks (size, cycles to failure) in the past 50 years. There are now several sophisticated computer codes for crack propagation calculations such as DARWIN®, NASGRO®, and AFGROW. These codes have many man-years of investment in algorithm development, materials characterization and code verification. However, at best these codes can be used in a design mode or an after the fact analysis given a download of the data from an engine. Currently, trained neural networks are used to implement a mechanical or material degradation in order to get real-time performance. However, neural networks must be trained for each particular situation and cannot model the capabilities in today's and tomorrow's fracture mechanics codes.

***In order to get real-time performance and use the sophisticated fracture mechanics knowledge, we will implement a probabilistic fracture mechanics algorithm in hardware to facilitate real-time estimation of crack behavior and structural integrity.***

Since it is unlikely that the complete level of sophistication of the today's fracture mechanics codes with many man-years of investment can be programmed in hardware in a short amount of time, a particular challenge will be to determine the most significant elements of the probabilistic fracture mechanics algorithm. These elements will then be the focus of the hardware implementation.

The objective of this research is to develop and test an ASIC (Application Specific Integrated Circuit) that implements a probabilistic fracture mechanics algorithm for real-time assessment of structural integrity of engine components. The initial focus will be on gas turbine engine disks, however this technology is pervasive and therefore could be extended to other engine components, as well as other structural systems, e.g., airframes, off-shore structures.

The algorithm, implemented in hardware, will provide a real-time probability of fracture estimate for the engine component (initial focus is the disk) given loading inputs, material properties, initial crack size estimate and other inputs, see technical details below, using LCF crack propagation fracture mechanics.

The objectives are phased over three years with the effort of years 2 and 3 dependent on the outcome of previous year's efforts. A flowchart of the deterministic fracture



mechanics is shown in Figure 2.1. The elements of the algorithm are discussed as follows:

- A) Input from existing sensors (RPM, temperature, vibration, power level angle)
- B) Crack sensor input – estimates location and size
- C) Stress transformation – determines stresses from sensor inputs from A.
- D) Rainflow analysis – determines damage increments
- E) Material property inputs – crack growth data ( $da/dN$ )
- F) Fatigue life model – calculate crack growth increment
- G) Input from crack sensor regarding current crack size
- H) Failure analysis
- I) Life estimate

Rainflow is the name given to the method of determining stress reversals that will cause fatigue crack growth. (A stress reversal represents a fatigue cycle from a min-max-min or max-min-max stress values.) A balanced rainflow algorithm, neither including nor excluding too many stress reversals, is critical to having a real-time on-board system. Including too many stress reversals would negatively affect the performance of the system and may prevent a real-time application. Excluding damaging stress reversals will be nonconservative.

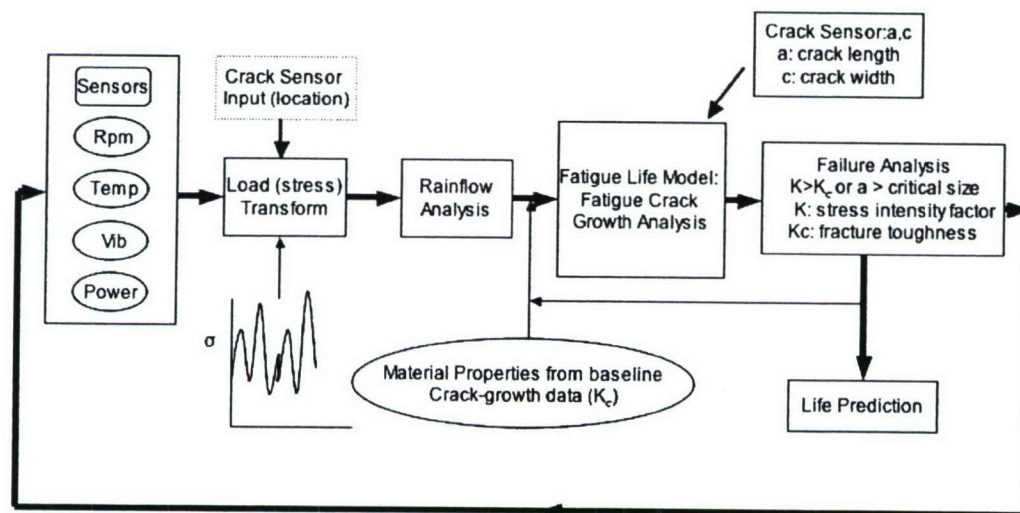


**Figure 2.1 Flowchart of deterministic fatigue algorithm**

In the following sub-sections, the algorithms for data filtering and rainflow counting are explained.

## 2.2 Data Filtering Process

The beginning step in a fatigue analysis for variable-amplitude loading such as engine rpm data is to determine a compact form of loading data that is composed of multiple sequences by peaks and valleys. A counting of rainflow pairs is easy by using filtered loading data, and calculation time is also saved in a real-time application. In this sub section, a new simple algorithm for data filtering process is suggested and demonstrated using a sample data and a real engine data.

### 2.2.1 Procedure

The fundamental idea of a data filtering process is to select the peaks and valleys from a variable-amplitude loading. In order to accomplish a data filtering process, following two steps are required.

- A. First, eliminate all intermediate values between peaks and valleys, and
- B. Secondly, eliminate all repeating magnitude.

Some technical computer programming steps are explained in the next section 2.2.2, by using a sample test data.

### 2.2.2 Example

A sample test data is shown in Table 2.1 that contains 15 loading steps with positive stress data.

**Table 2.1 Sample data of variable-amplitude loading**

Loading steps	1	2	3	4	5	6	7	8	9	10	11	12	13	14	15
Stress data	0	2	2	2	5	5	5	9	6	6	7	4	4	8	9

The peaks and valleys stress data can be obtained, 0-9-6-7-4-9 by insight from the sample data in Table 2.1. To obtain these peaks and valleys numerically, it is required to calculate the numerical difference in magnitude between two consecutive points. A detailed procedure is explained as followong, and summarized the results in Table 2.2. The Diff\_1 and Diff\_2 in Table 2.2, represent differences, say current and previous difference, respectively. The next step is to determine a slope of each Diff\_1 and Diff\_2 for checking a slope change occurrence. The sign 1 means a positive slope, 0 for a zero slope, and -1 for a negative slope, respectively. The last step is to modify the slope to eliminate same intermediate slopes, using the sign of Diff\_1 and Diff\_2. The rules for a modification slope in the last step are:

[sign(diff\_1)=1 and sign(diff\_2)=0] → 1,  
[sign(diff\_1)=-1 and sign(diff\_2)=0] → -1,  
[sign(diff\_1)=0 and sign(diff\_2)=0] and [sign(diff\_1-1)=1] → 1,  
[sign(diff\_1)=0 and sign(diff\_2)=0] and [sign(diff\_2-1)=1] → 1,  
[sign(diff\_1)=0 and sign(diff\_2)=0] and [sign(diff\_1-1)=-1] → -1,  
[sign(diff\_1)=0 and sign(diff\_2)=0] and [sign(diff\_2-1)=-1] → -1,



The last row, End\_sign in Table 2.2 shows the modified slope. The peaks and valleys, 0-9-6-7-4-9 can be obtained by a selection of the stress when a slope change has occurred, with keeping beginning and end stress values.

**Table 2.2 Data filtering scheme of variable-amplitude loading (15 points)**

Loading	1	2	3	4	5	6	7	8	9	10	11	12	13	14	15
Stress	0	2	2	2	5	5	5	9	6	6	7	4	4	8	9
Diff 1	*	2	0	0	3	0	0	4	-3	0	1	-3	0	4	1
Diff 2	2	0	0	3	0	0	4	-3	0	1	-3	0	4	1	*
Sign(diff 1)	*	1	0	0	1	0	0	1	-1	0	1	-1	0	1	1
Sign(diff 2)	1	0	0	1	0	0	1	-1	0	1	-1	0	1	1	*
End_sign	*	1	1	1	1	1	1	-1	-1	1	-1	-1	1	1	*

\* beginning and ending

points

This technique is very simple and effective to determine only the peaks and valleys for any kinds of data sequence, and easy to write a program. Figure 2.2 shows the data reduction results schematically using Matlab, by using the sample test data of Table 2.1.

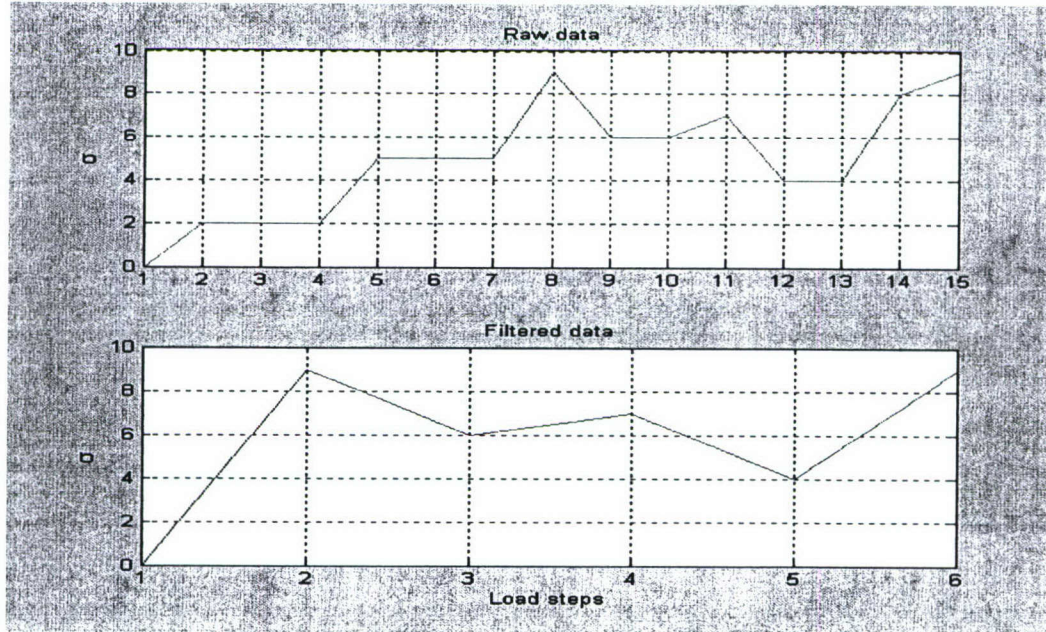


**Figure 2.2 Comparison of raw data filtered data using 15 test data**

The data reduction process is also demonstrated to a real engine data. In the Figure 2.3, the first graph represents a raw stress data from engine rpm, and the second graph shows only peaks and valleys data, which is filtered from 11,360 raw data to 256 points. It can be understood that there is many repeated data with the same value and with unnecessary intermediate data between peaks and valleys. The filtered points are only consisted of peaks and valleys like shown a zoomed box in the second graph, Figure 2.3.

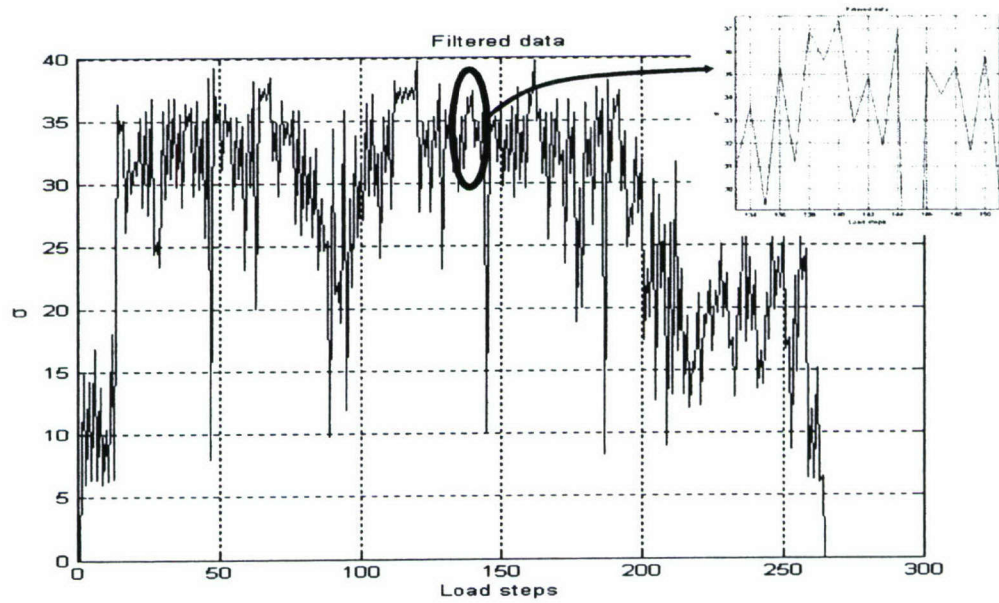
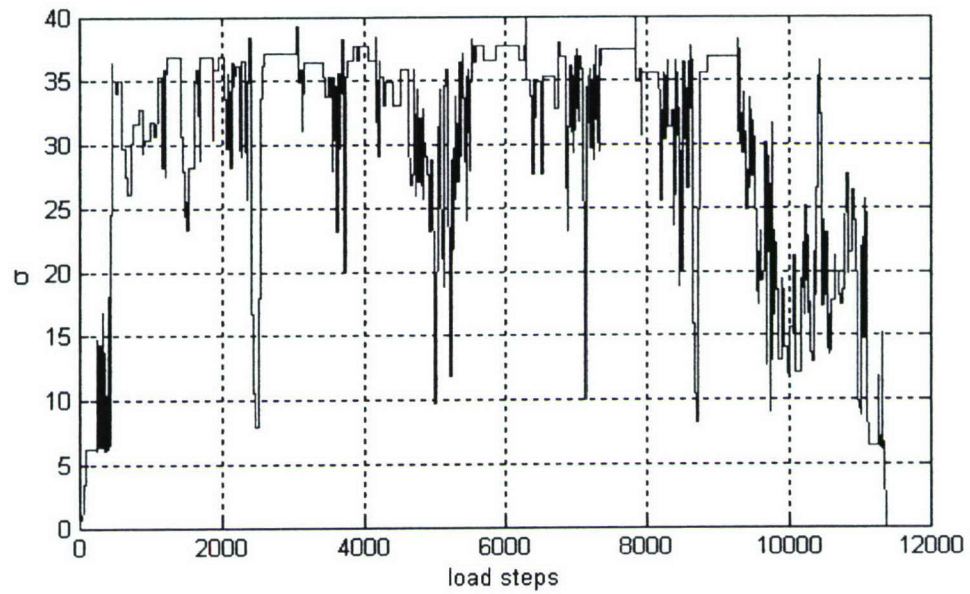


**Figure 2.3 Comparison of original raw data filtered data using real engine data**



## 2.3 Rainflow Cycle Counting (Range-Pair Method)

In order to improve rainflow cycle counting for a real-time data input and analysis, a range-pair method is chosen. The advantages of range-pair method are that it is simple to apply an algorithm because of comparing just three consecutive points, and it may pick up many rainflow pairs before sub-iteration, to find remaining rainflow pairs.

### 2.3.1 Cycle-Extraction Method

- 1) Define  $k_1$ ,  $k_2$ , and  $k_3$  from the stress  $\Delta\sigma_2$  data without data reordering.
- 2) Define two stress ranges using three consecutive points:  

$$\Delta\sigma_1 = |\sigma_{k_2} - \sigma_{k_1}|, \Delta\sigma_2 = |\sigma_{k_3} - \sigma_{k_2}|$$
- 3) Extract two points  $k_1$ ,  $k_2$  (peak and valley points) if the condition,  $\Delta\sigma_1 \leq \Delta\sigma_2$  is satisfied.
- 4) Define three new consecutive points,  $k_1=k_3$ ,  $k_2=k_{1+1}$ ,  $k_3=k_{1+2}$  when condition  $\Delta\sigma_1 \leq \Delta\sigma_2$  is satisfied.
- 5) Define three new consecutive points  $k_1=k_2$ ,  $k_2=k_{1+1}$ ,  $k_3=k_{1+2}$  when condition  $\Delta\sigma_1 \leq \Delta\sigma_2$  is not satisfied.
- 6) Perform until last points, and one reversal counting for the last three points, in other words, extract  $k_2$ ,  $k_3$  if the condition  $\Delta\sigma_1 \geq \Delta\sigma_2$  is satisfied.
- 7) Perform sub-iteration using remaining points which are called residue, to find out the stress pairs which are generated by residue.

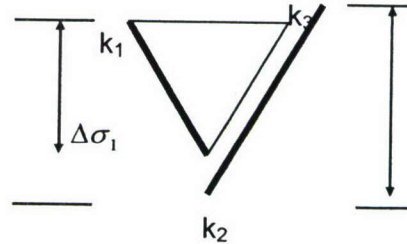


Figure 2.4 Definition of stress range

### 2.3.2 Verification

#### ASTM E1049-85 test sample data

ASTM test data is chosen to validate the developed range-pair rainflow counting method. Figure 2.5 represents the ASTM data and result, which has 9 original data and 4 rainflow pairs. The magnitude and cycle of rainflow pairs are sketched by each black triangle. The magnitude of each rainflow pair is 3(A-B), 4(E-F), 8(C-D), 6(H-I) respectively. Each rainflow pair in Figure 2.6 represents UTSA result. From Figures 2.5-2.6, rainflow pairs are exactly matched in magnitude and cycles.

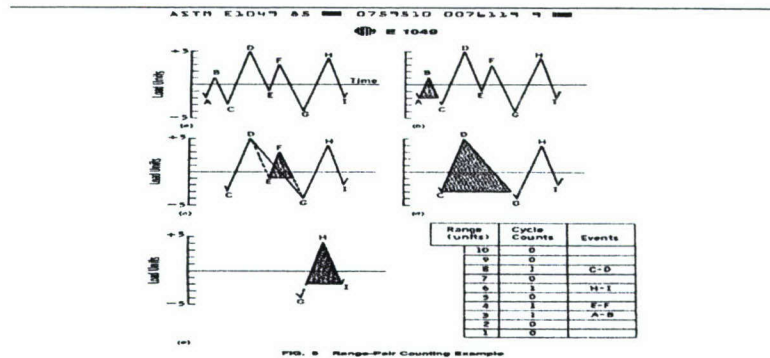


Figure 2.5 ASTM rainflow test results [4]

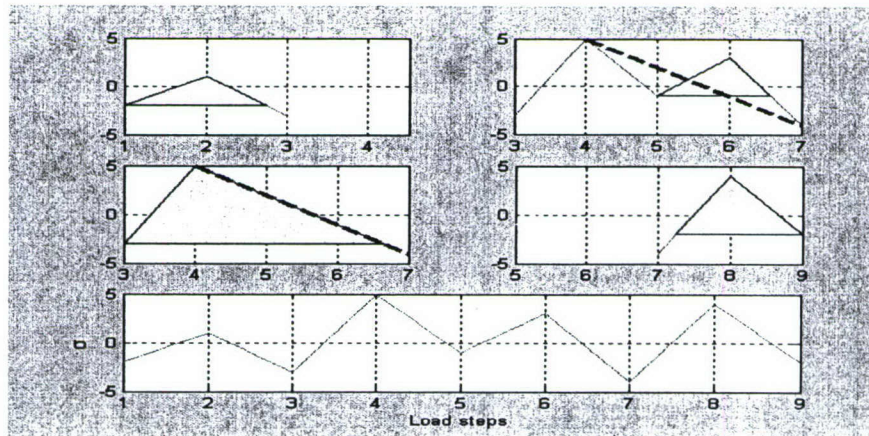


Figure 2.6 Rainflow test results using UTSA

### Real engine data (Air-to-Ground)

This sub-section is introduced to verify the developed code UTSA to a real engine data. Unlike the sample test data, there is a huge number of input data. Darwin is used to compare the rainflow pairs with UTSA. The magnitude of stress pairs is not equal in each program since different rainflow counting methods are adopted in each code (simplified rainflow method for Darwin, range-pair method for UTSA). The total number of rainflow pairs is same, 132 for both UTSA and Darwin. There is no need that the total number of rainflow pairs should be the same for each code. The big difference between UTSA and Darwin rainflow sequence is that UTSA uses incoming order of data by real time acquisition, but Darwin modifies the sequence of order by swapping the maximum stress pairs locate at the beginning.

Figure 2.7 represents a  $\Delta\sigma$  ( $\sigma_{\max} - \sigma_{\min}$ ) comparison from the rainflow pairs output between UTSA and Darwin by ascending order. From this figure, UTSA and Darwin show almost the same magnitude of sigma difference at each rainflow pair. The detailed comparisons in a specific region are depicted in Figures 2.8-2.10. A sigma difference shows the exact same values between UTSA and Darwin in a range of rainflow pairs, 1~12 (Figure 2.8), and UTSA a little higher than Darwin in a range of rainflow pairs, 61~72 (Figure 2.9) and Darwin a little higher than UTSA in a range of rainflow pairs, 121-132 (Figure 2.10).



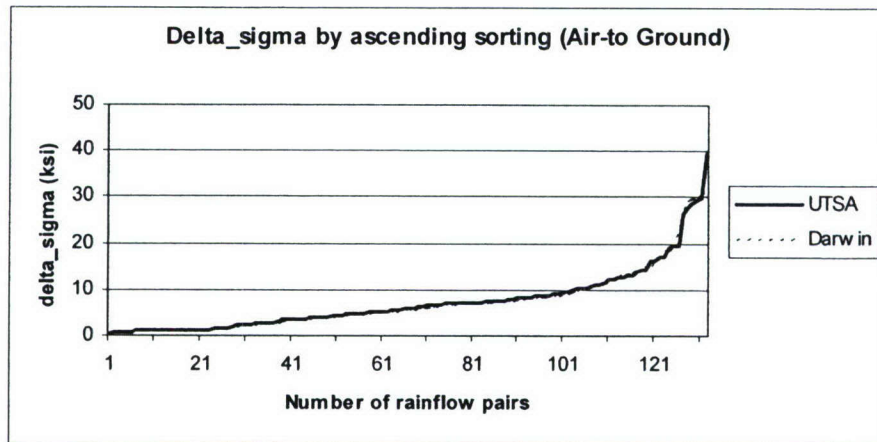


Figure 2.7 Comparison of  $\Delta\sigma$  by ascending order

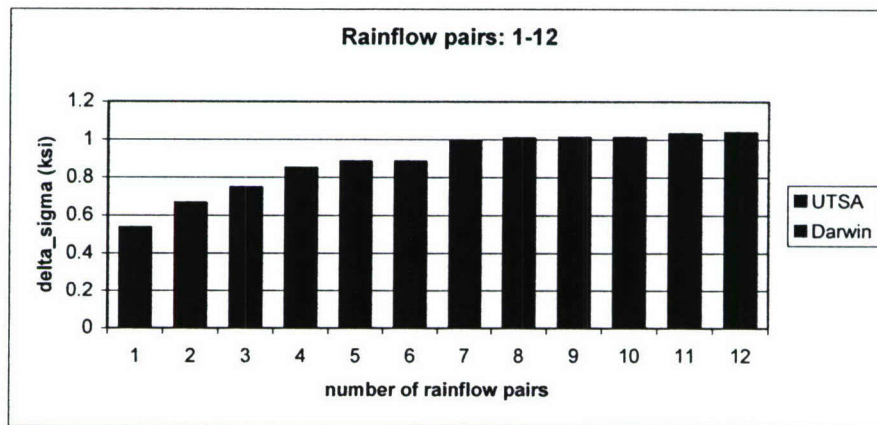


Figure 2.8 Comparison of  $\Delta\sigma$  by ascending order, 1-12

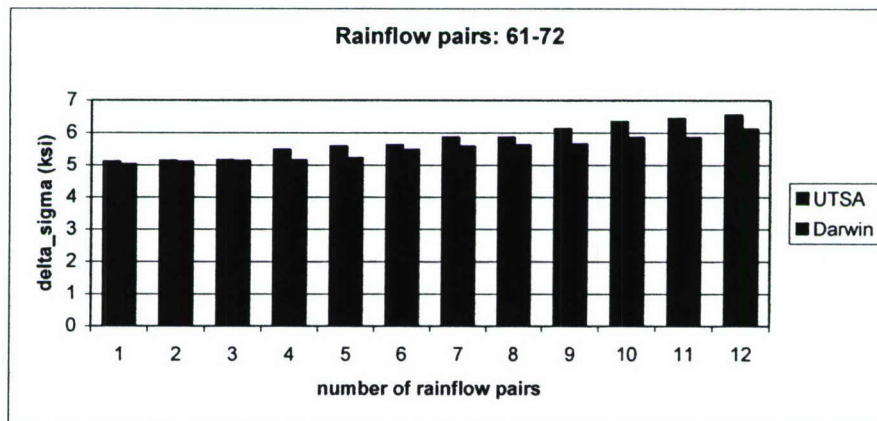


Figure 2.9 Comparison of  $\Delta\sigma$  by ascending order, 61-72

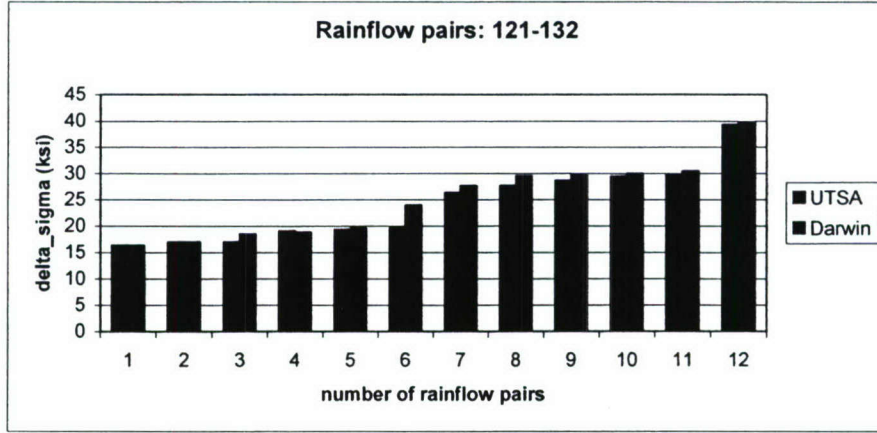


Figure 2.10 Comparison of  $\Delta\sigma$  by ascending order, 121-132

## 2.4 Fatigue Analysis

In order to verify the crack growth by fatigue analysis using the developed code UTSA, constant amplitude loading (test data) and variable-amplitude loading (real engine data) are considered. Paris law is utilized for UTSA to simplify the fatigue analysis. Darwin and AFGRO are used to compare the crack growth results.

### 2.4.1 Paris Law

The simple algorithm of Paris law is introduced, and evaluated in UTSA. Stress intensity is defined as following.

$$\Delta K = K_{\max} - K_{\min} \quad (2.4.1)$$

In a surface crack,  $K$  varies along the crack perimeter. Therefore, complete characterization of crack growth requires description of both crack shape (length, width) and size. In this research, a noncircular crack shape is considered in determining  $K$ , in equation (2.4.2).

$$K = \sigma \sqrt{\pi a(c)} \beta \quad (2.4.2)$$

Where,  $\beta$  is the dimensionless geometry factor. From an equation (2.4.2),  $K_{\max}$  and  $K_{\min}$  are defined as followings.

$$\begin{aligned} K_{\max} &= \sigma_{\max} \sqrt{\pi a(c)} \beta \\ K_{\min} &= \sigma_{\min} \sqrt{\pi a(c)} \beta \end{aligned} \quad (2.4.3)$$

$\sigma_{\max}$  and  $\sigma_{\min}$  are the maximum and minimum stress at each rainflow pairs that can be obtained from rainflow counting. By inserting equations (2.4.1-2.4.3) into a Paris law,  $\frac{da}{dN} = c_{\text{paris}} (\Delta K)^{m_{\text{paris}}}$ , an incremental crack growth can be calculated.



$$\Delta a(c) = c_{\text{paris}} * \Delta K^{m_{\text{paris}}} * \Delta N$$

$$a(c) = a(c) + \Delta a(c) \quad (2.4.4)$$

The surface crack shape and dimension are represented in Figure 2.11.

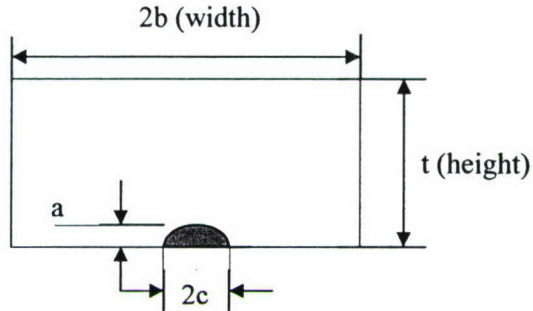


**Figure 2.11 Surface crack shape and dimension in a finite plate**

## 2.4.2 Verification

### 2.4.2.1 Constant Amplitude Loading

One simple example of constant amplitude loading is examined to verify the developed code UTSA. Geometry dimension and material properties are summarized in Table 2.3. The magnitude of constant loading is 80 ksi, with an initial value 0 ksi.

**Table 2.3 Geometry and material properties**

Crack growth rate	Paris law
Initial crack size	a=c=0.2
Fracture toughness	58.0
Constants for Paris law	c <sub>paris</sub> =2.325e-09; m <sub>paris</sub> =3.0594
Specimen dimension	width=height=10
Crack type	surface crack(Darwin: SC02)
Material property	Darwin : ti64_Paris_closure.mat
Cycles	10

#### Crack growth rate

Figure 2.12 represents the crack growth, with respect to number of cycles. From these figures, UTSA and Darwin results show very good agreement. A normalized comparison is represented in Figure 2.13, by setting UTSA=1.

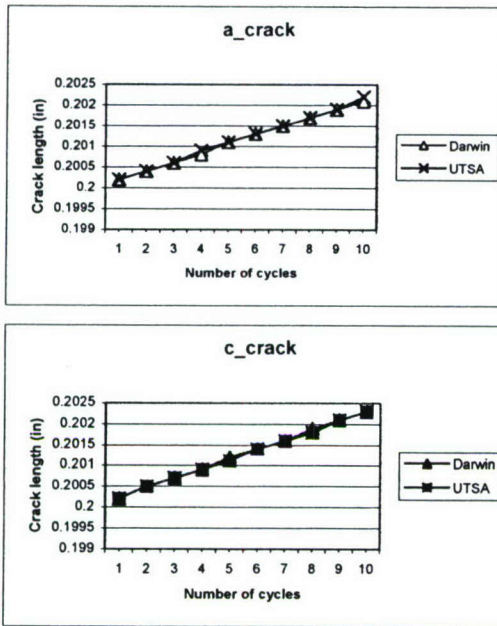


Figure 2.12 Comparison of a\_crack with respect to cycles

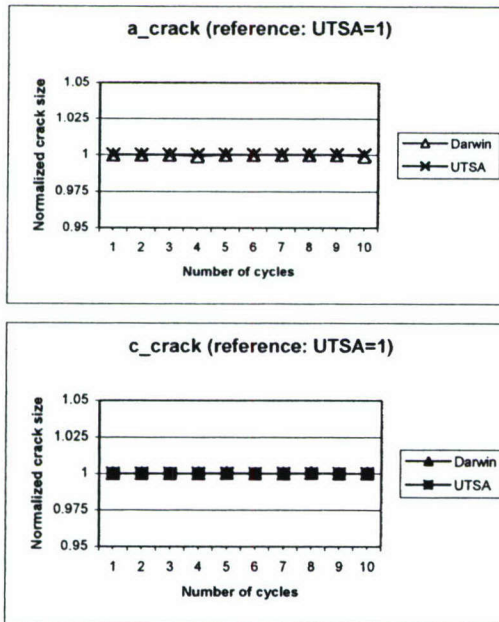
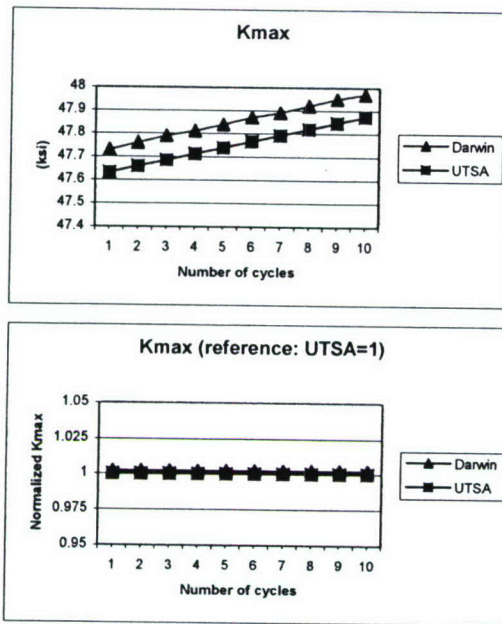


Figure 2.13 Normalized comparison of crack growth with factor, UTSA=1

K<sub>max</sub> (Maximum of stress intensity factor)

Figure 2.14 represents K<sub>max</sub> and normalized values comparison. UTSA and Darwin show very close results.





**Figure 2.14 Comparison of Kmax and normalized values with cycle increase**

Dimensionless geometry factor,  $\beta$

Figure 2.15 represents a dimensionless geometry factor,  $\beta$  solution. UTSA and Darwin show very close results to c-direction, but Darwin shows almost constant value, 0.75, for both directions.

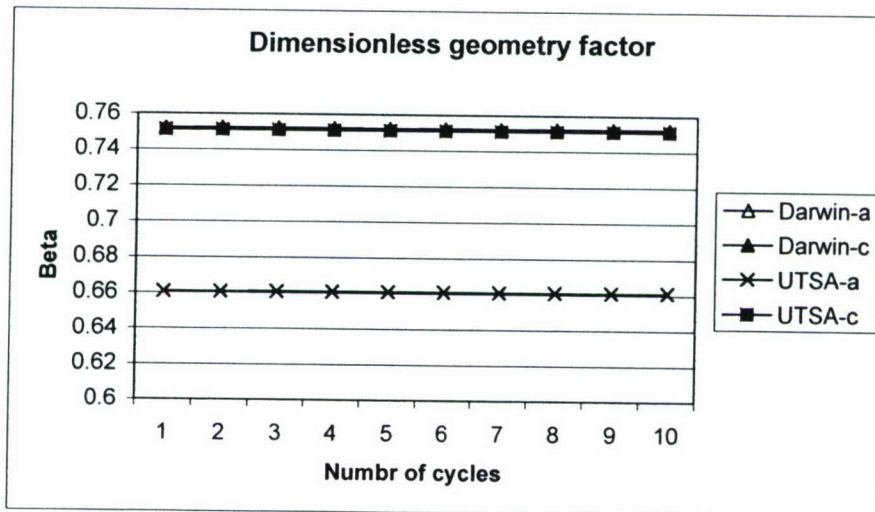


**Figure 2.15 Comparison of  $\beta$  with flight number increase**

### 2.4.2.2 Variable-Amplitude Loading (real engine data: Air to Ground)

For a variable-amplitude, three softwares (UTSA, Darwin, AFGROW) are applied to compare the crack growth,  $K_{max}$ , and dimensionless geometry factor,  $\beta$ . An initial crack size is assumed 0.3, and 10 flight number is assumed. Other geometry and material properties are summarized in Table 2.4.

**Table 2.4 Geometry and material properties**

Crack growth rate	Paris law
Initial crack size	$a=c=0.3$
Fracture toughness	58.0
Constants for Paris law	$c_{\text{paris}}=2.325e-09$ ; $m_{\text{paris}}=3.0594$
Specimen dimension	width=height=10
Crack type	surface crack(Darwin: SC02, AFGROW:Center semi_elliptic surface flaw)
Material property	Darwin : ti64_Paris_closure.mat AFGROW: ti 6Ai-4V
Flight numbers	10

#### Crack growth rate

Figures 2.16-12.18 represent the crack growth results in both directions. Darwin shows faster crack growth, and AFGROW shows slower crack growth than others. UTSA and UTSA\_D (using Darwin stress pairs and running UTSA code) show almost the same results, and their results are between Darwin and AFGROW results. There is a little weak point to compare directly AFGROW with other results since the material used is not the same, as mentioned in Table 2.4. By comparing with Figures 2.16-2.18,  $c_{\text{crack}}$  grows faster than  $a_{\text{crack}}$ . A normalized comparison is represented in Figure 2.17, by setting  $UTSA=1$ . Both cracks show very little percentage difference, say within 1%.

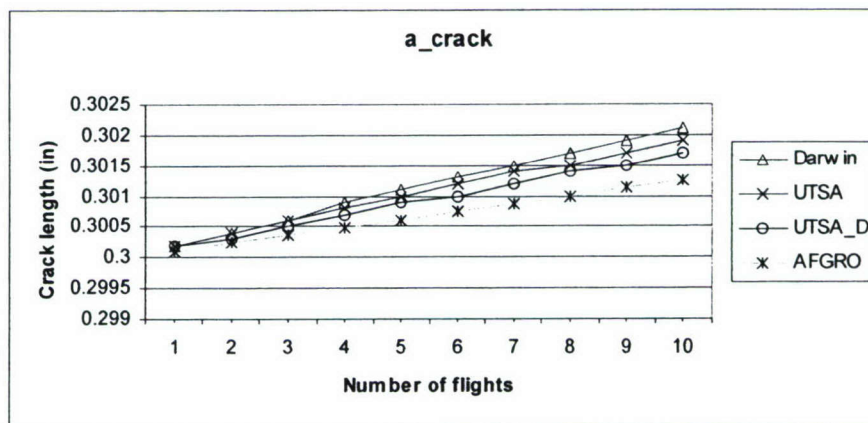


**Figure 2.16 Comparison of  $a_{\text{crack}}$  with flight number increase**



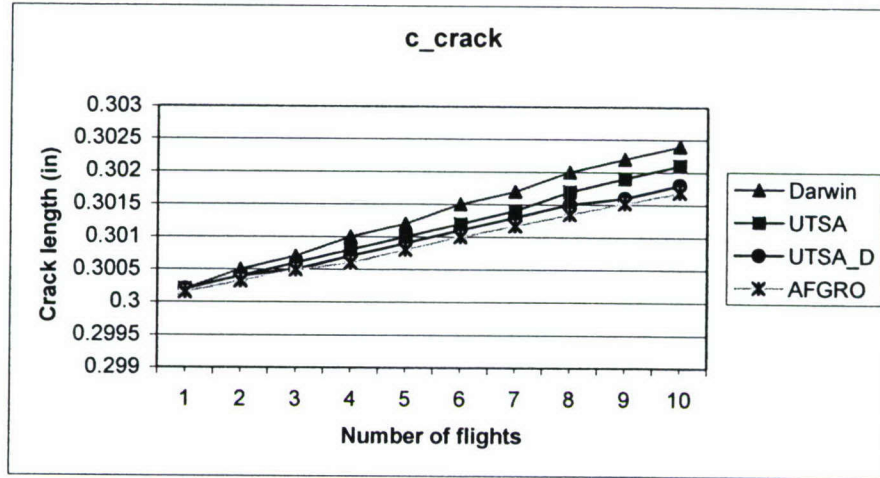


Figure 2.17 Comparison of  $c\_crack$  with flight number increase

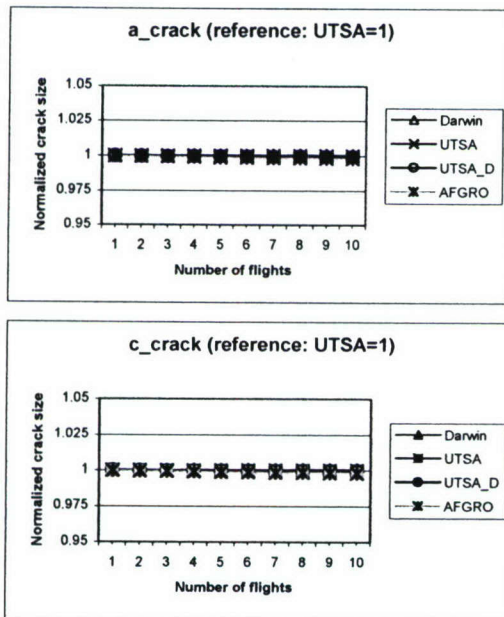


Figure 2.18 Normalized comparison of crack growth with factor,  $UTSA=1$

### K<sub>max</sub>

Figures 2.19-2.20 represent  $K_{max}$  and normalized value comparison. AFGROW shows approximately 5% lower values relative to other cases, and Darwin, UTSA, and UTSA\_D show very close results.

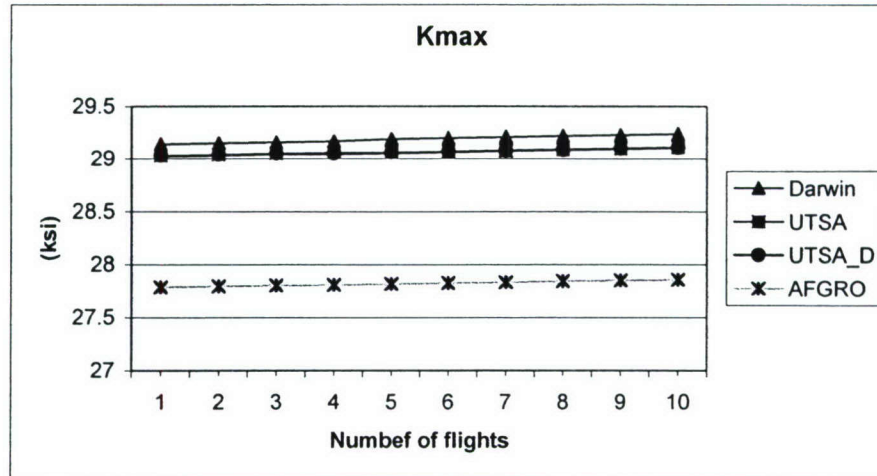


Figure 2.19 Comparison of Kmax with flight number increase

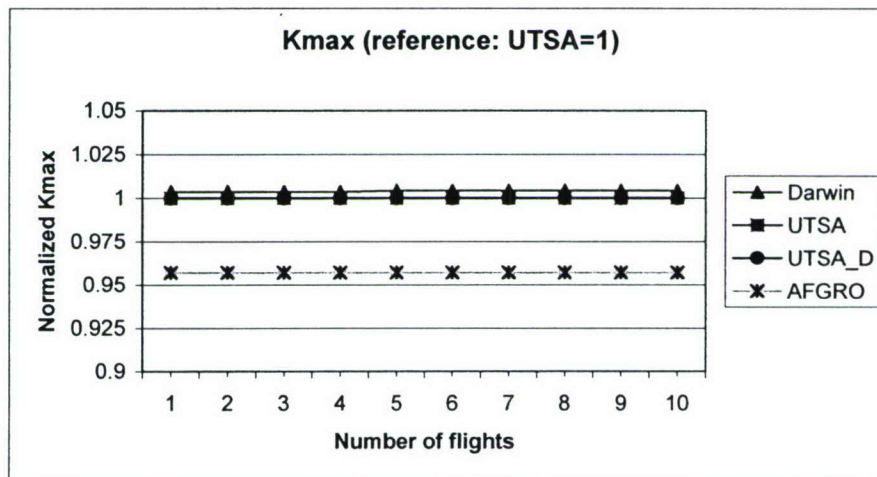


Figure 2.20 Normalized comparison of Kmax with with factor, UTSA=1

Dimensionless geometry factor,  $\beta$

Figure 2.21 represents a dimensionless geometry factor,  $\beta$  solution. UTSA-c, UTSA\_D-c, Darwin-a, and Darwin-c show the largest value in the top line. UTSA-a, UTSA\_D-a, and AFGROW-a show the smallest value in the bottom line.



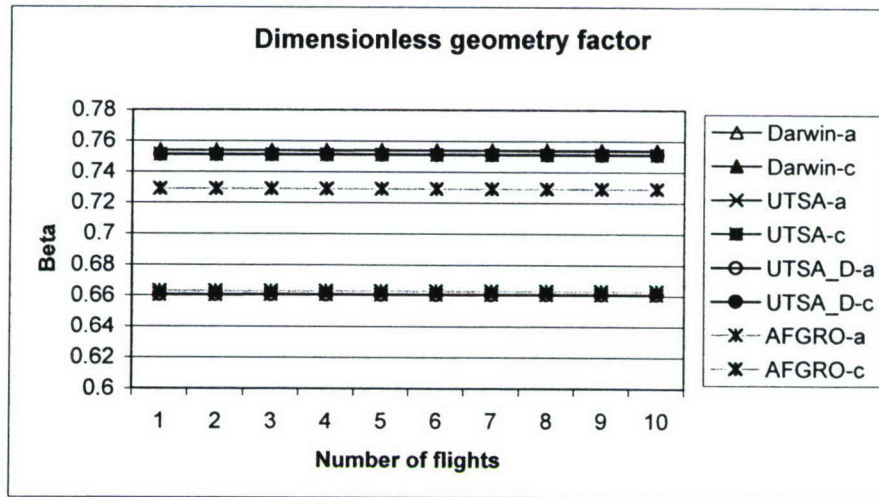


Figure 2.21 Comparison of  $\beta$  with flight number increase

### 2.4.2.3 Various Mission Types

In this subsection, various missions (Instrument & Navigation, Functional Check Flight, Live Fire Missiles, Target Tow, Air to Ground, Live Fire, Transition and proficiency) are considered about crack growth rate,  $K_{max}$  using UTSA and Darwin. Figures 22-28 represent a crack grow rate, and Figures 29-35 represent a  $K_{max}$ . All results show very good agreement between Darwin and UTSA. In the legend, D means Darwin and U means UTSA code results.

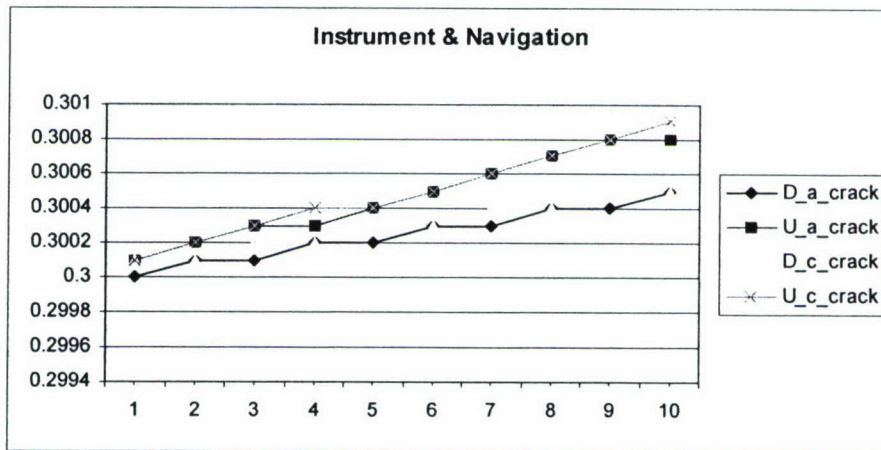
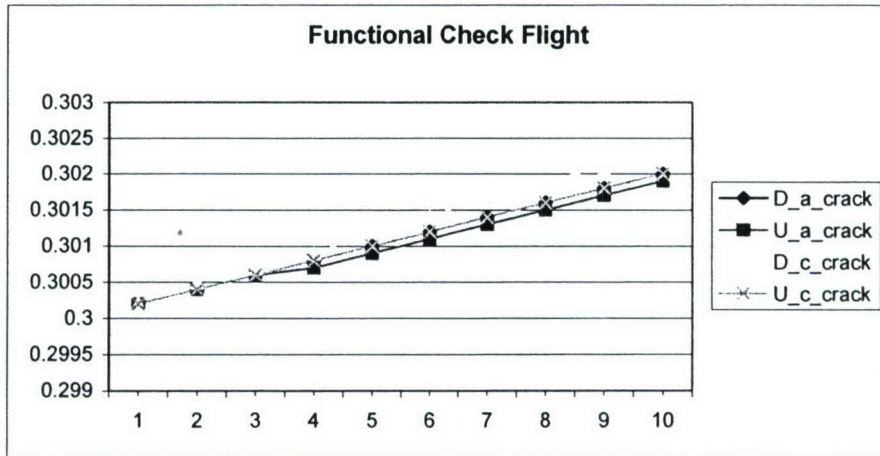
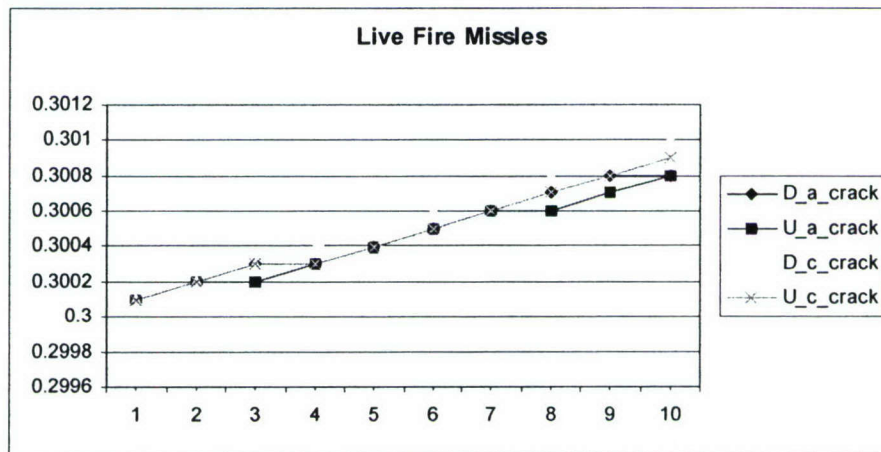


Figure 2.22 Comparison of a crack growth rate with flight number increase



**Figure 2.23 Comparison of a crack growth rate with flight number increase**



**Figure 2.24 Comparison of a crack growth rate with flight number increase**

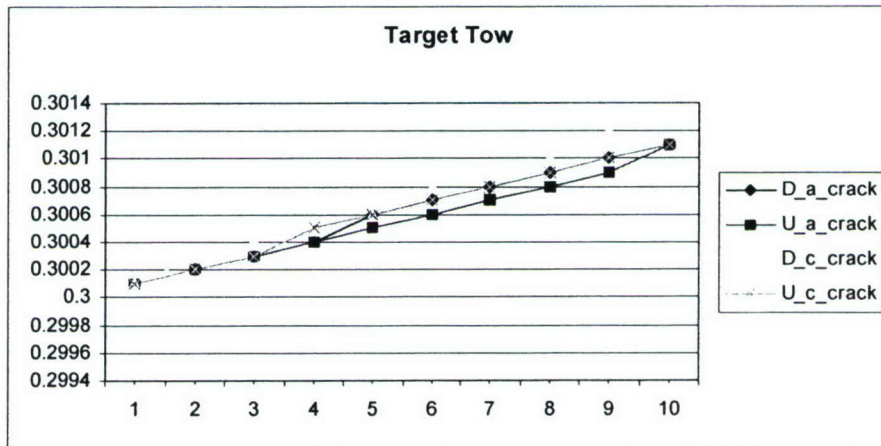


**Figure 2.25 Comparison of a crack growth rate with flight number increase**



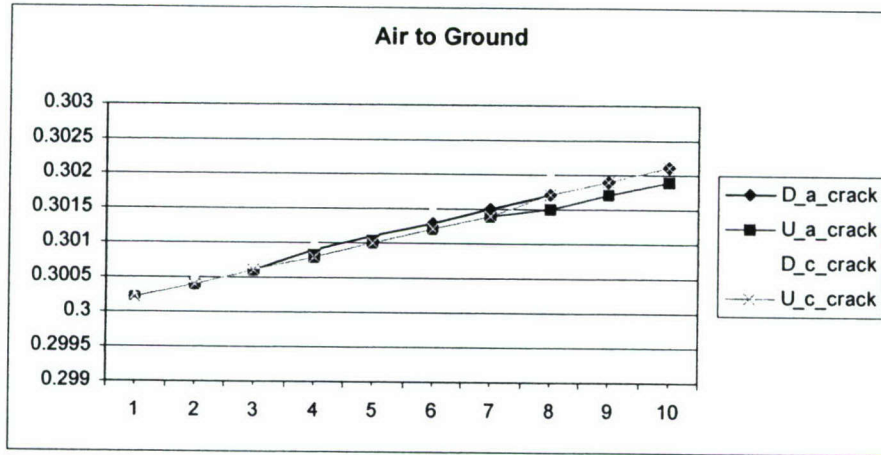


**Figure 2.26 Comparison of a crack growth rate with flight number increase**



**Figure 2.27 Comparison of a crack growth rate with flight number increase**

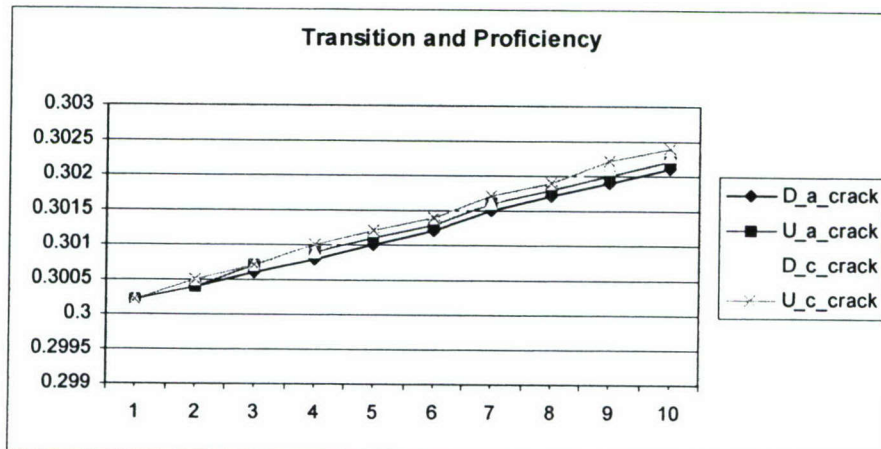


**Figure 2.28 Comparison of a crack growth rate with flight number increase**

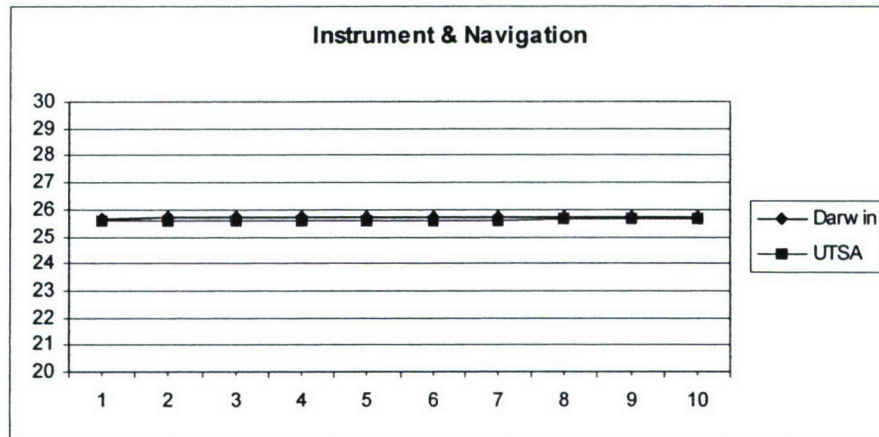


**Figure 2.29 Comparison of Kmax with flight number increase**

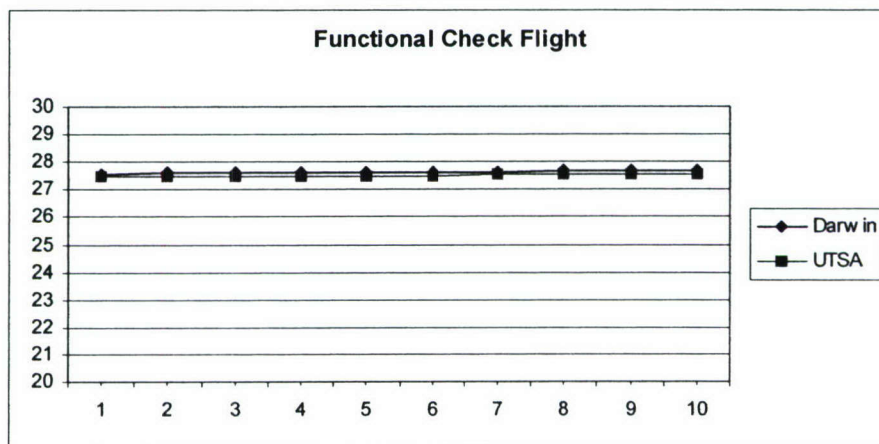


**Figure 2.30 Comparison of Kmax with flight number increase**

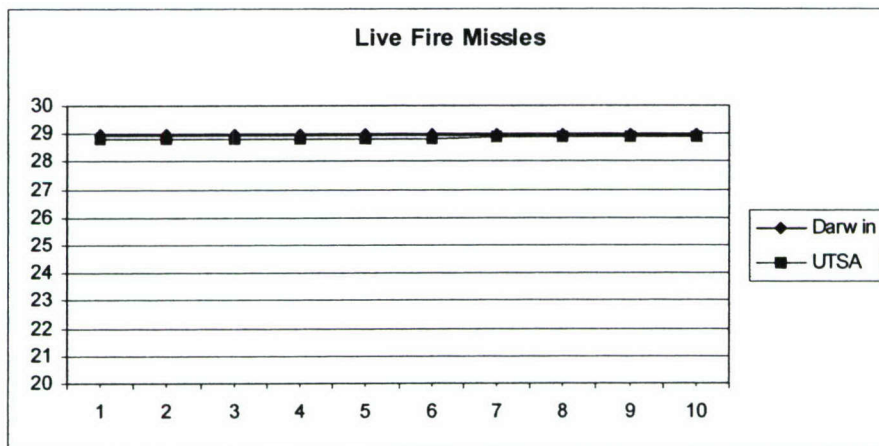


**Figure 2.31 Comparison of Kmax with flight number increase**



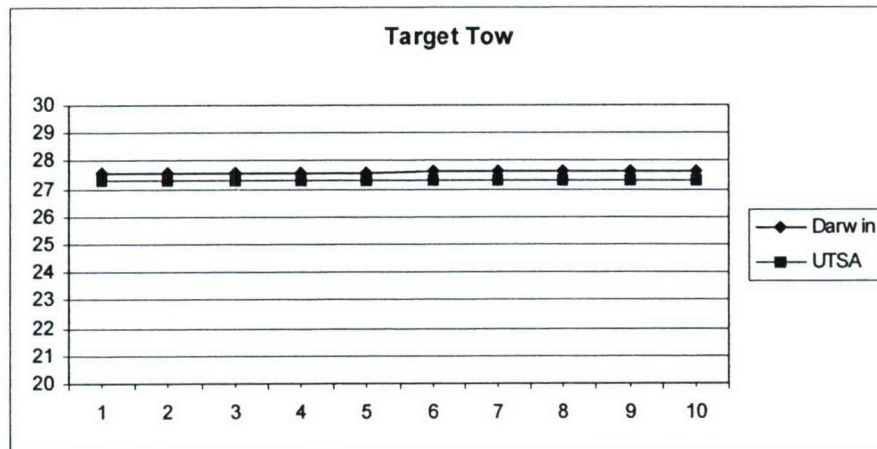


**Figure 2.32 Comparison of Kmax with flight number increase**

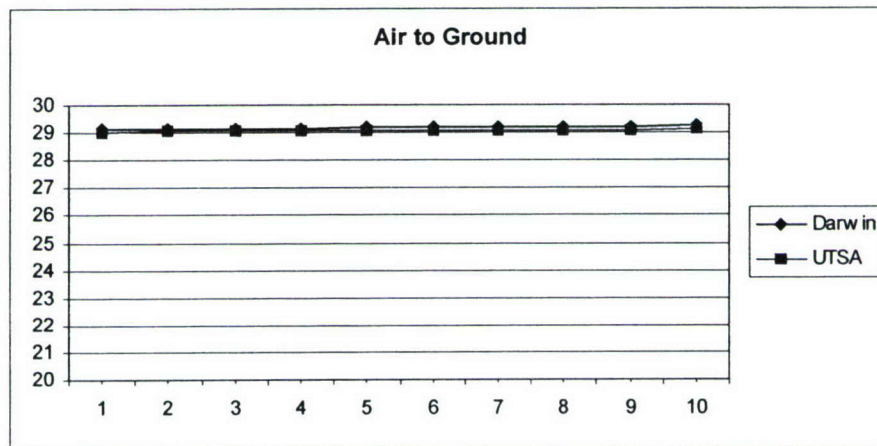


**Figure 2.33 Comparison of Kmax with flight number increase**

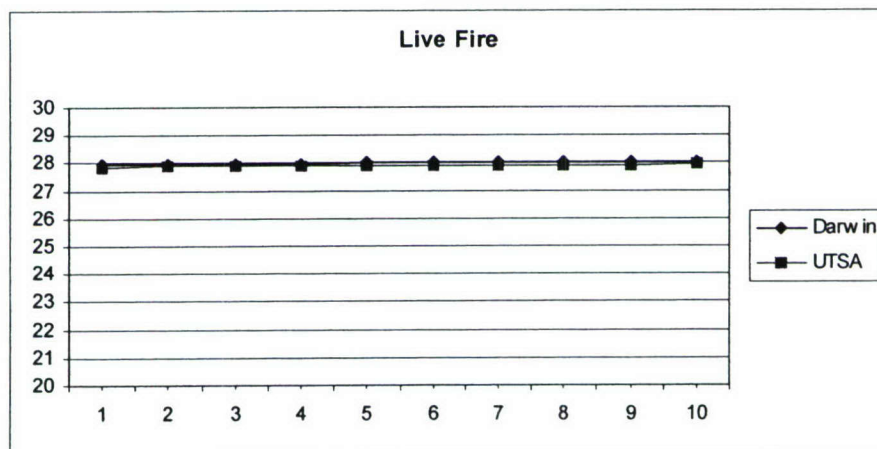


**Figure 2.34 Comparison of Kmax with flight number increase**

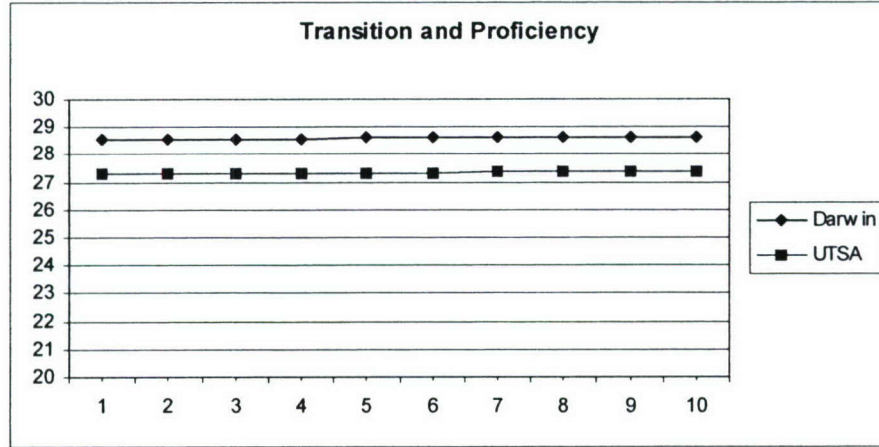


**Figure 2.35 Comparison of Kmax with flight number increase**

## 2.5 Monte Carlo Simulation

The statistical model is imbedded in a Monte Carlo simulation [6] to assess the impact of uncertainty and variability. In a deterministic analysis, the loading results are used as an input to a damage model, such as a fatigue model. The life of the engine therefore can then be evaluated at different stress levels. The use of Monte Carlo simulation in the evaluation process can overcome this problem. In this research, the uncertainty from stress input is considered, and the stress data was calculated from the given rpm data using following equation (2.5.1).

$$Stress = ref\_stress * rpm / ref\_rpm \quad (2.5.1)$$

The chosen reference stress value and reference rpm are 113ksi and 14,300 respectively.

In order to compensate uncertainty of stress data, random numbers were generated by log normal distribution, and multiplied by stress values.

$$Stress = Stress * Sigma\_error \quad (2.5.2)$$

In equation (2.5.2), a term of Sigma\_error is represented by standard deviation and mean values which have log normal distribution.

$$\begin{aligned} Std\_dev &= \sqrt{\log(1 + cov^2)} \\ Mean &= \log(median\sqrt{1 + cov^2}) - 0.5\log(1 + cov^2) \end{aligned} \quad (2.5.3)$$

The median and coefficient of variance are 1.0 and 5%, respectively.

### 2.5.1 Histogram

Figures 2.36–2.40 represent histograms of a-crack, c-crack, crack area for sample 100, 500, 1000, 5000, and 10000 after 10 flights. An initial crack size was assumed, 0.1 in.



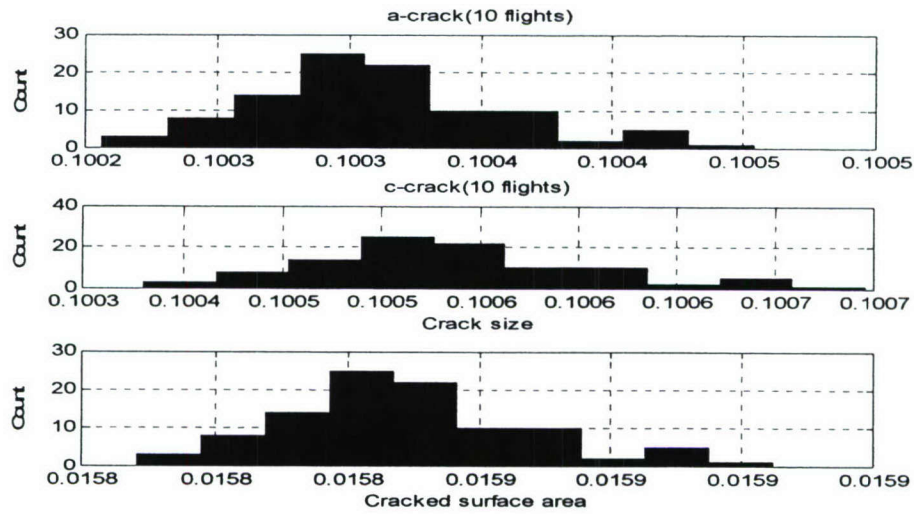


Figure 2.36 Histogram for sample 100

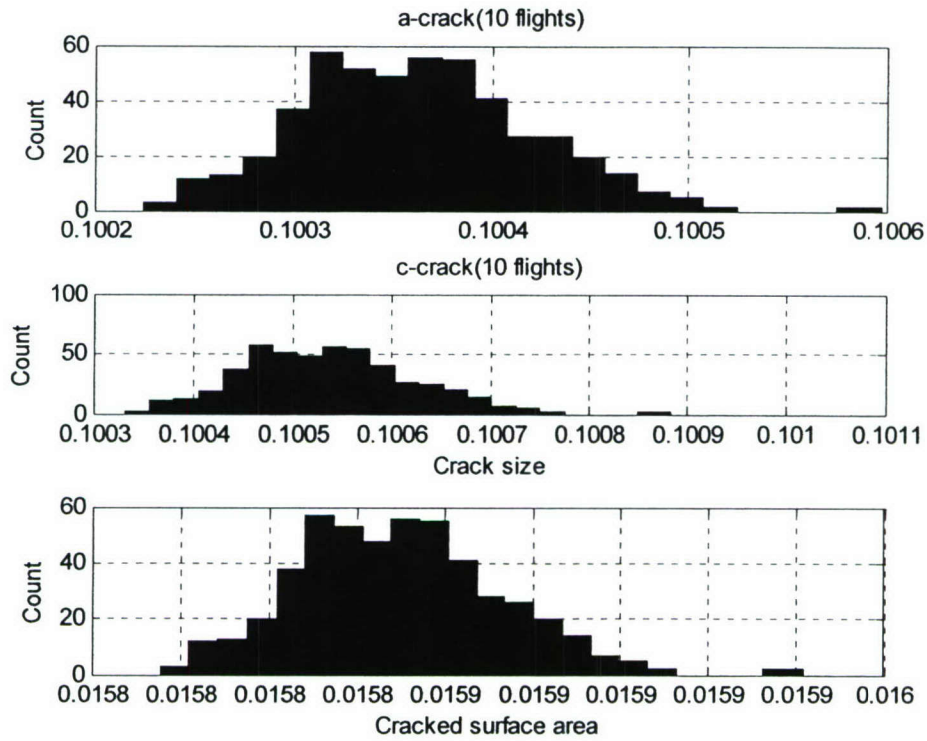
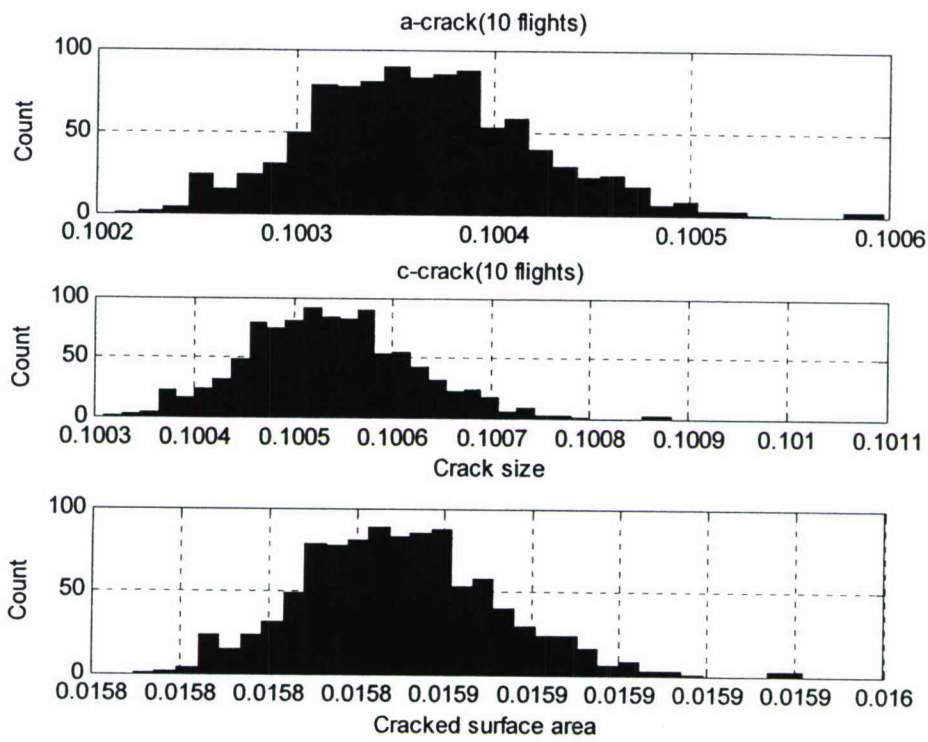
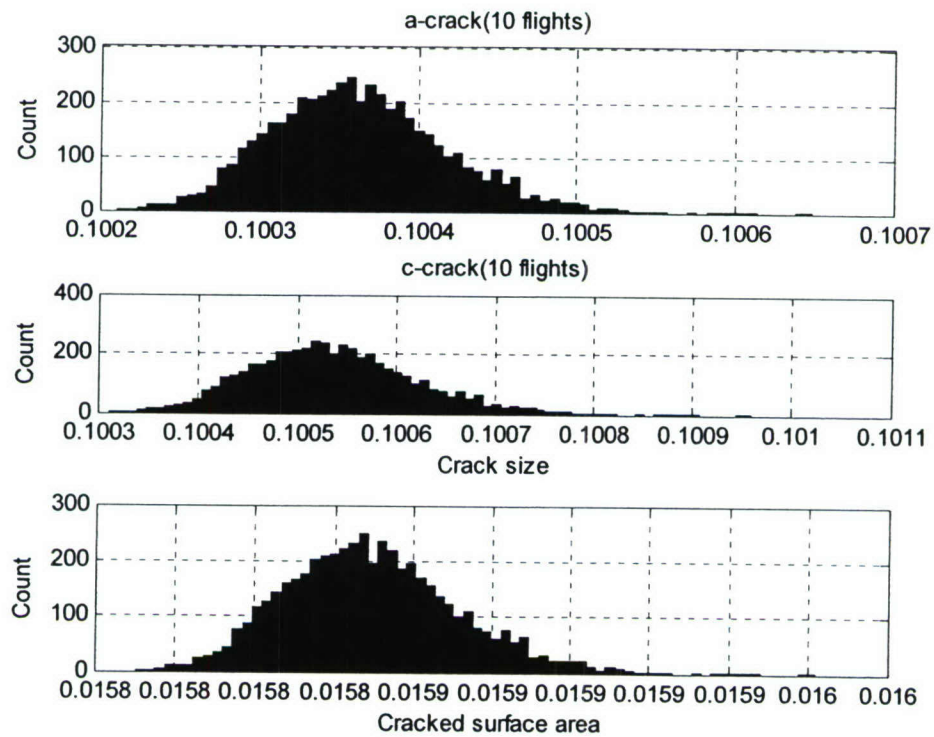


Figure 2.37 Histogram for sample 500



**Figure 2.38 Histogram for sample 1000**



**Figure 2.39 Histogram for sample 5000**

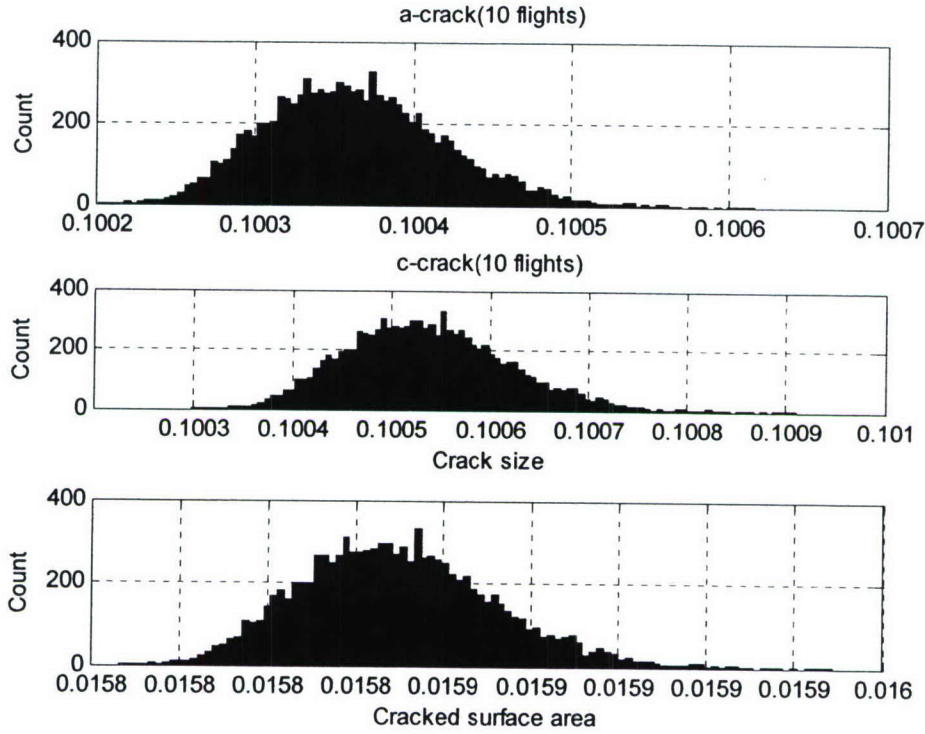


Figure 2.40 Histogram for sample 10000

## 2.5.2 Kernel Density Distribution

In this subsection, kernel density distribution is introduced to plot each histogram by a density distribution. Density distribution is needed to study a Bayesian updating process in the next chapter. Following four different kernels (2.5.4) [7] were compared in efficiency by defining efficiency of K as (2.5.5).

$$\text{Epanechnikov} \quad \frac{3}{4} \left(1 - \frac{1}{5}t^2\right) / \sqrt{5} \quad \text{for } |t| < \sqrt{5}, \quad 0 \text{ otherwise}$$

$$\text{Triangular} \quad 1 - |t| \quad \text{for } |t| < 1, \quad 0 \text{ otherwise}$$

$$\text{Normal} \quad \frac{1}{\sqrt{2\pi}} e^{-(1/2)t^2}$$

(2.5.4)

$$\text{Rectangular} \quad \frac{1}{2} \quad \text{for } |t| < 1, \quad 0 \text{ otherwise}$$

$$\text{eff}(K) = \{C(k_e) / C(K)\}^{5/4} = \frac{3}{5\sqrt{5}} \left\{ \int t^2 K(t) dt \right\}^{-1/2} \left\{ \int K(t)^2 dt \right\}^{-1} \quad (2.5.5)$$

From comparison of efficiency [7], there is very little to choose between the various kernels on the basis of mean integrated square root. In this research, normal kernel is



chosen without specific reason. Figure 2.41 represents a data plot to evaluate data continuation when random numbers are generated for various samples by ascending order. Horizontal axis means the total sample numbers and vertical axis means a-crack size distribution. Figure 2.42 shows a distribution of crack area using normal kernel with respect to various sample numbers. More smooth density distribution can be obtained as increase of sample numbers.

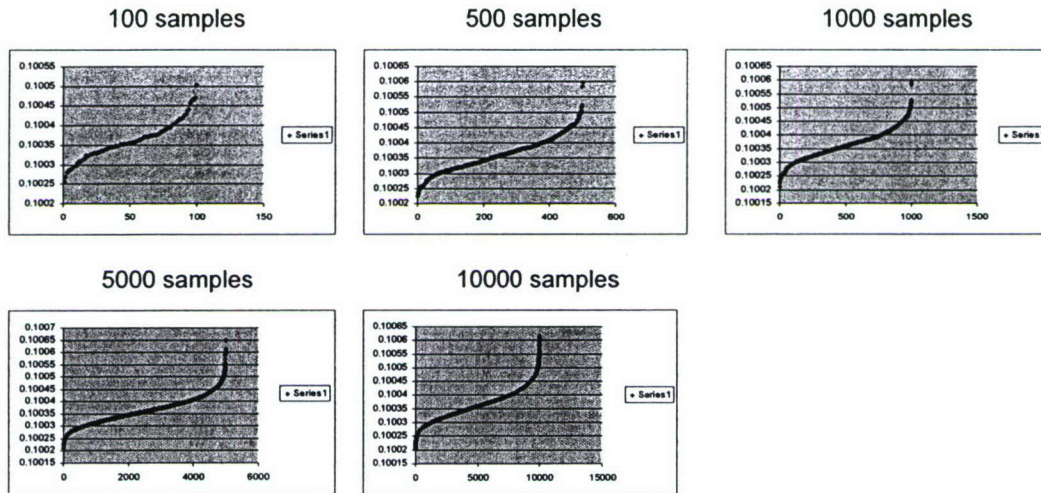


**Figure 2.41 Crack data plot by ascending order for various sample numbers.**

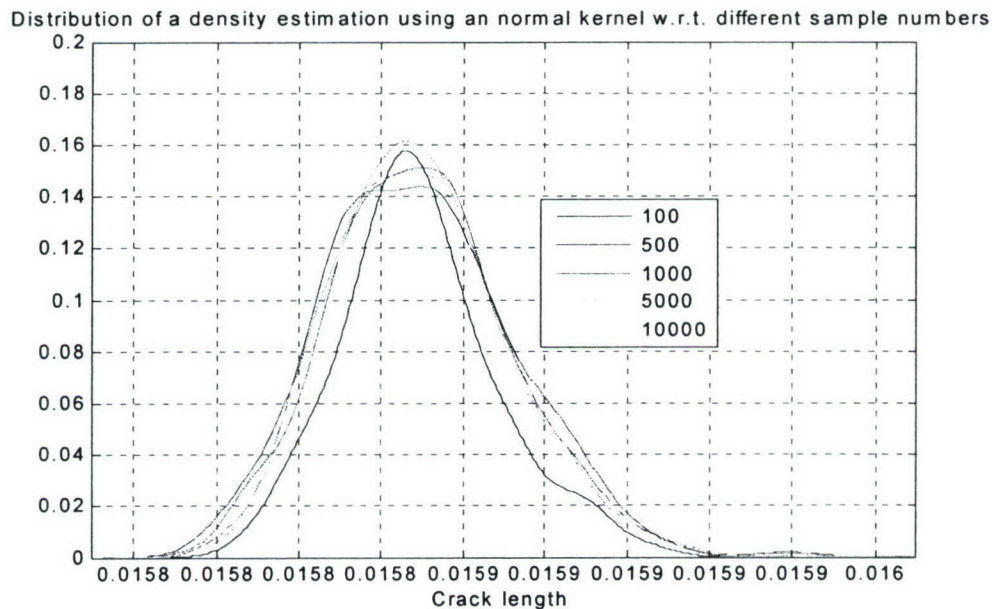


**Figure 2.42 Distribution of a density estimation of crack area using normal kernel with respect to various sample numbers**

### 2.5.3 Test for Bayesian Updating

If the value of a parameter can be represented as a continuous PDF, the prior assumptions on the parameter can be formally updated by Bayes' theorem [8]. If  $\varepsilon$  is an observed experimental results, the prior distribution  $f'(\theta)$  can be revised in the light of experimental results using Bayes' theorem. Let  $\theta$  be the random variable for the parameter of a distribution, posterior probability that will be in  $(\theta_i, \theta_i + \Delta\theta)$  as

$$f''(\theta_i)\Delta\theta = \frac{P(\varepsilon | \theta_i)f'(\theta_i)\Delta\theta}{\sum_{i=1}^n P(\varepsilon | \theta_i)f'(\theta_i)\Delta\theta} \quad (2.5.6)$$

where  $P(\varepsilon | \theta_i) = P(\varepsilon | \theta_i < \theta \leq \theta_i + \Delta\theta)$ . In the limit, this yields

$$f''(\theta_i) = \frac{P(\varepsilon | \theta_i)f'(\theta_i)}{\int_{-\infty}^{\infty} P(\varepsilon | \theta_i)f'(\theta_i)d\theta} \quad (2.5.7)$$

The term  $P(\varepsilon | \theta_i)$  is the likelihood of observing the experimental outcome  $\varepsilon$  assuming that the value of the parameter is  $\theta$ . This is commonly referred to as the likelihood function of  $\theta$  and denoted  $L(\theta)$ , and denominator (normalizing constant,  $k$ ) is independent of  $\theta$ . Then,

$$\begin{aligned} f''(\theta) &= kL(\theta)f'(\theta) \\ k &= \left[ \int_{-\infty}^{\infty} L(\theta)f'(\theta)d\theta \right]^{-1} \end{aligned} \quad (2.5.8)$$

In order to test a Bayesian updating process, two test cases are considered. The first case is to use a textbook sample, and the second case is to apply engine data.

#### 2.5.3.1 Test a Bayesian using a Textbook Sample [8]

Two examples are considered for testing a Bayesian updating. The first case is to use a uniform prior distribution (known as diffuse prior) and likelihood function, as seen in equations (2.5.9) and (2.5.10).

$$f'(\theta) = 1.0 \quad 0 \leq \theta \leq 1 \quad (2.5.9)$$

$$L(\theta) = \theta \quad (2.5.10)$$

By applying equation (2.5.8), the posterior distribution of  $\theta$  is

$$f''(\theta) = 2\theta \quad (2.5.11)$$

This example is very simple case, and Figure 2.43 represents the result using a developed Matlab code.

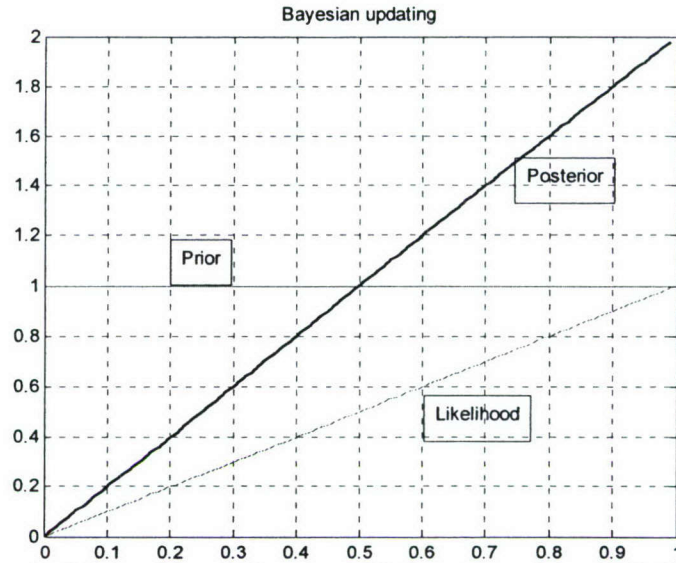


**Figure 2.43 Bayesian updating of distribution using a Matlab code**

The second example is that the prior distribution function and the probability of detection are assumed like as equation (2.5.12) and (2.5.13), respectively.

$$f'(\theta) = \begin{cases} 208.3\theta & 0 < \theta < 0.06 \\ 20 - 125\theta & 0.06 < \theta < 0.16 \\ 0 & \theta > 0.16 \end{cases} \quad (2.5.12)$$

$$P(\varepsilon | \theta_i) = \begin{cases} 0 & \theta < 0 \\ 8\theta & 0 < \theta < 0.125 \\ 1.0 & \theta > 0.125 \end{cases} \quad (2.5.13)$$

Figure 2.44 represents a Bayesian updating of a distribution using textbook sample using a developed Matlab code.

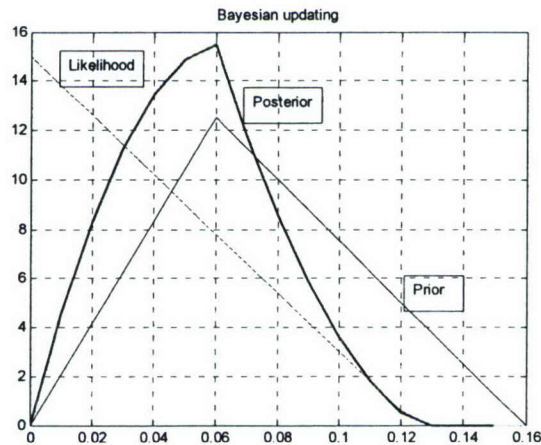


**Figure 2.44 Bayesian updating of distribution of flaw depth using a Matlab code**



Figure 2.45 shows textbook results. By comparing Figures 2.44-2.45, it shows good agreement in a posterior distribution.

342 BAYESIAN APPROACH

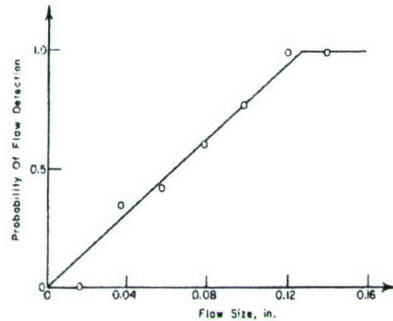


Figure 8.3 Detectability versus actual flaw depth (data from Packman et al., 1968)

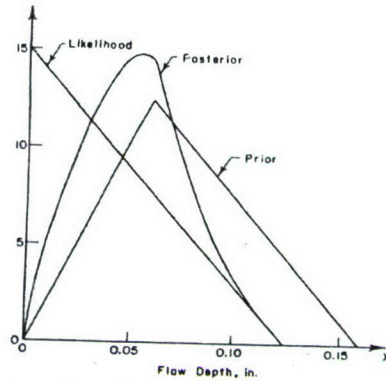


Figure E8.6 Distribution of flaw depth

Figure 2.45 Bayesian updating of distribution of flaw depth [8]

### 2.5.3.2 Test a Bayesian using a Real Engine Data

The 10<sup>th</sup> flight a-crack data is assumed as a prior distribution function,  $f'(\theta)$  and the 10<sup>th</sup> flight c-crack data is assumed as likelihood function  $L(\theta)$ . This approximated function of a probability of detection is used for current research because of not achieving likelihood data from sensor. It is assumed that we can obtain better posterior distribution as long as we can obtain a real data from sensor. Figure 2.46 represents a prior and likelihood distribution when 10000 samples were used.

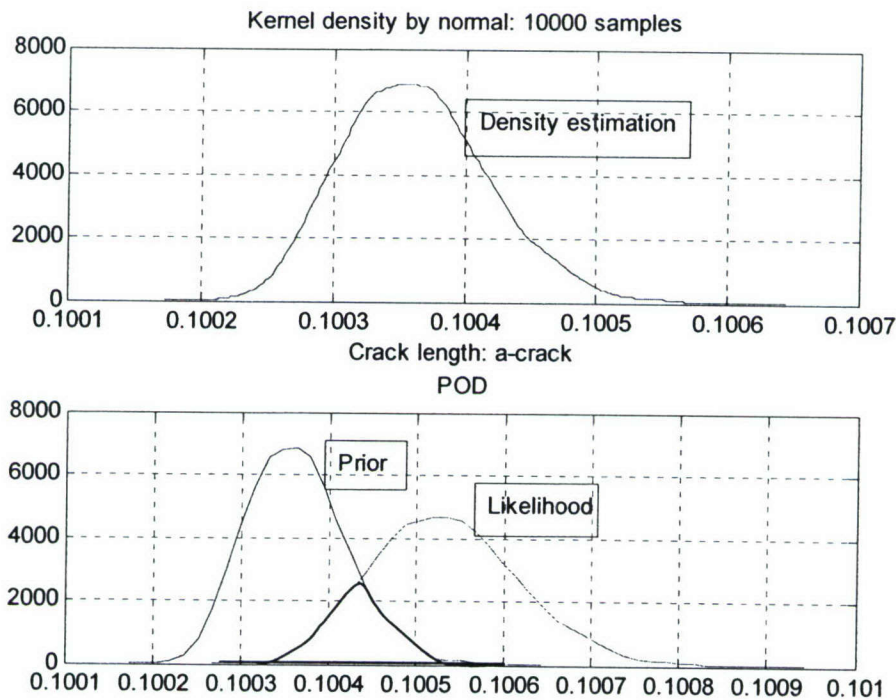
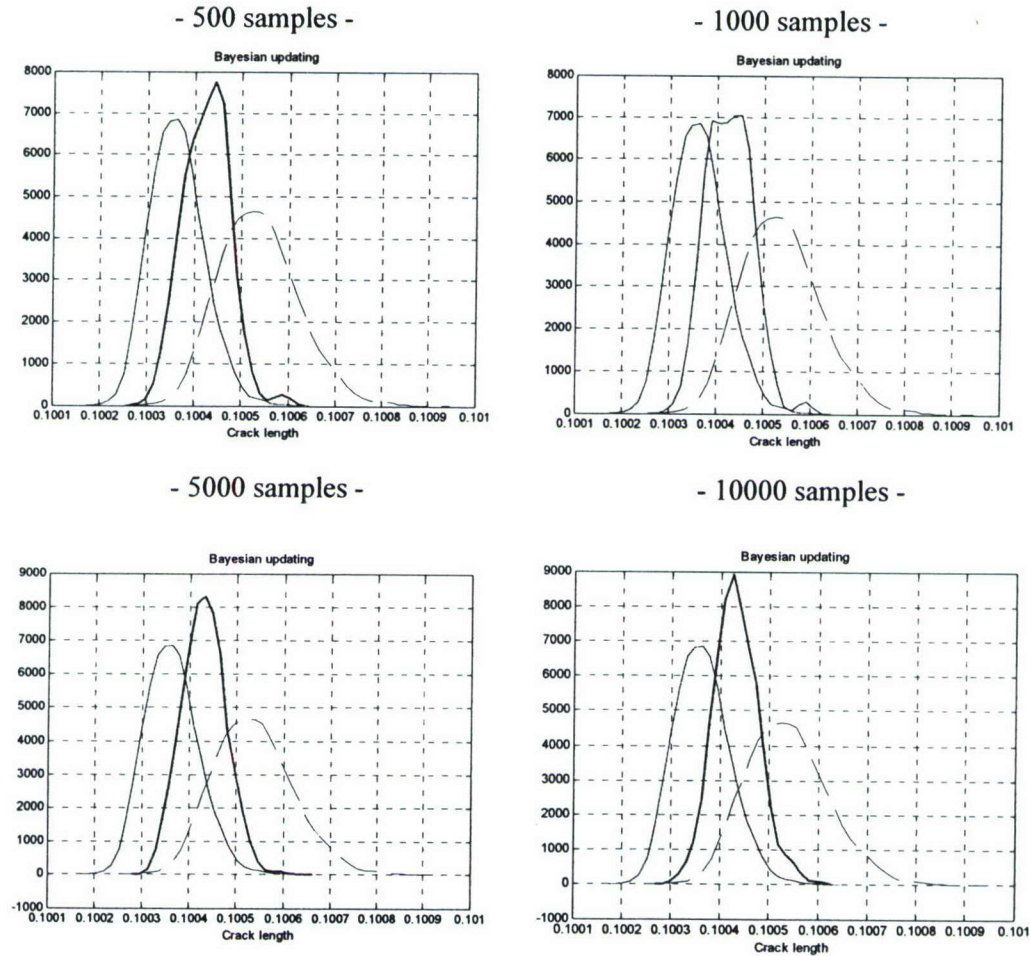


Figure 2.46 Bayesian updating of distribution of flaw depth

A linear or nonlinear fitting of density functions is required to predict a posterior distribution since Bayesian updating can be performed by multiply a prior distribution with a likelihood distribution, as shown in equation (2.5.8). In order to multiply by two fitting functions within overlapping range (yellow region in Figure 2.46), each segment should have same integral length. The developed Matlab code can automatically recognize the overlapping range of prior and likelihood functions, then calculate posterior distribution using equation (2.5.8). Figure 2.47 represents a posterior distribution with respect to various sample size.



**Figure 2.47 Posterior distribution with respect to various sample sizes**

## 2.6 On Board Testing for Real Time Demonstration

Central to the idea of using embedded processors for monitoring engine health is their ability to perform heavy computational loads in real time. The task of real time signal processing presents us with a dilemma. The faster one collects measurements of a continuous real-life process such as vibrations within a turbine engine, the faster a processor must perform the desired function, in our case Rainflow algorithm. A high rate of measurement (or sample rate) is absolutely necessary to represent the real life



process accurately. It falls to the embedded implementation to achieve the desired arithmetic function within an acceptable sample rate. The implementation's sample rate performance can be evaluated by using code profiling methods. Prior to the hardware implementation, concept modeling was performed on the algorithm in Matlab using script functions. The results obtained from these models were made available in numerical and graphical form. Verification of hardware results requires using similar numeric and graphic methods.

### 2.6.1 Methods

Two design methods were explored. The first method was not used for the final implementation. It involved exploring an automated conversion from Matlab code to C code. The second was the final and preferred method for the implementation. It involved manual conversion of Matlab code to C code for executing on the TI DSP processor TMS320C6713. This method was successful in meeting the project objectives; implementation of fatigue analysis for life prediction on a prototype on-board health analysis system. Items purchased in regard to the hardware implementation objective are listed below, Table 2.5.

**Table 2.5 Materials list**

Item	Quantity	Cost
Matlab toolbox: Embedded Target for TI DSP	1	\$500.00
Matlab toolbox: Link for Code Composer Studio	1	\$200.00
TMS320C6713 DSP Starter Kit (DSK) rev C	1	\$400.00
TMS320C671 DSP Starter Kit (DSK)	1	\$400.00
<b>Total</b>		<b>\$1,500.00</b>

### 2.6.2 Real Time Animation Using Code Composer Studio

Rainflow concept was modeled using Matlab scripting. The results from Matlab were used to verify the results computed from the TI DSP processor which shown in Figure 2.48. The output from the TMS320C67xx processor was viewed numerically in the stdout window and graphically using tool under Code Composer Studio, as seen in Figure 2.49. Figure 2.48-a represents an incoming rpm data that is equivalent to Figure 2.3, and Figure 2.49-b & c show the real time animation plot of crack growth propagation to a and c directions. From 11360 raw input data points sampled, 264 critical stress points were calculated within the Peak Detection stage. This is a 97% reduction of the raw data. Including in-flight and post-flight processes, 132 values were calculated for each parameter, 'a\_crack' and 'c\_crack'. The parameter 'a\_crack' increased from the initial value of 0.3000 to a final value of 0.3002. The parameter 'c\_crack' increased from the initial value of 0.3000 to a final value of 0.3003.



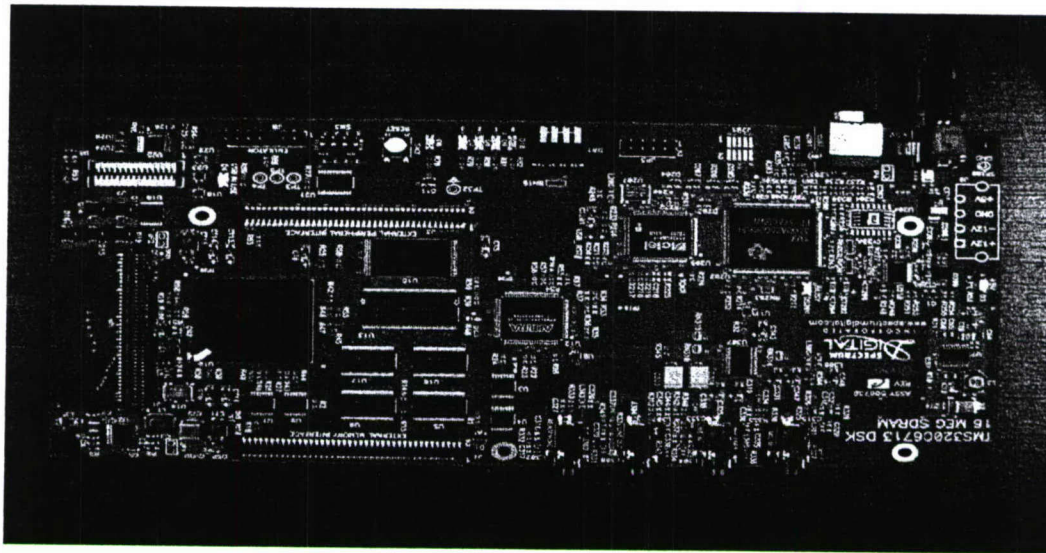
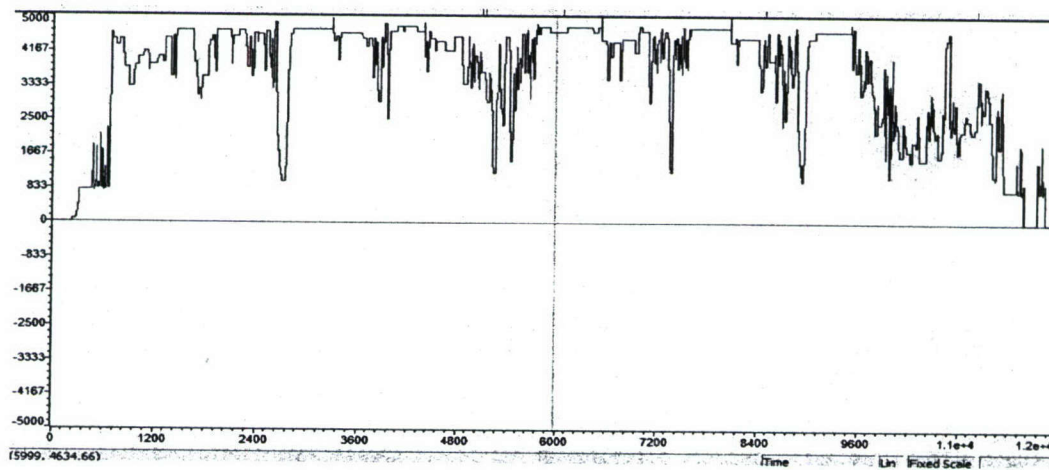
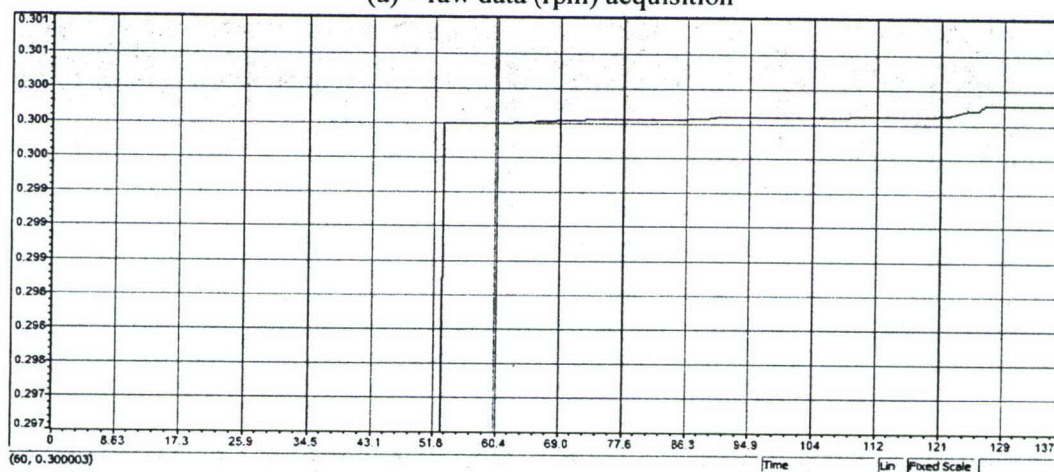


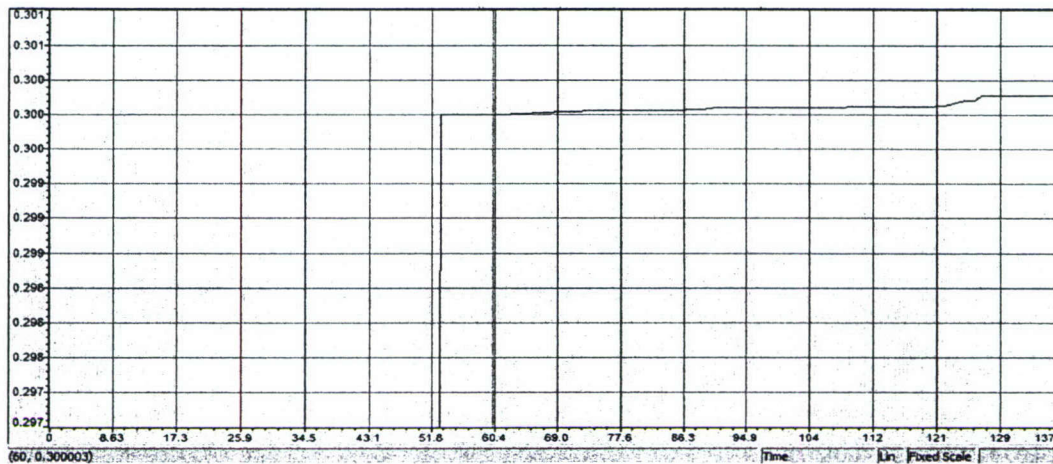
Figure 2.48 TMS320C6713 DSP Processor (16 Meg SDRAM)



(a) - raw data (rpm) acquisition



(b) - a crack propagation



(c) – c crack propagation

**Figure 2.49 Real time animation of data acquisition and crack propagation**

Figure 2.50 represents a test buffer size. Using buffer sizes in the range of 512 to 1024 is most efficient. Using buffer sizes greater than 1024 is an increasingly less efficient use of chip memory. These estimates are based on one type of flight data. Other benchmarks should be run to test different flight mission types. For example, a flight mission involving high-speed maneuvers produces greater number of stress reversals. This translates to an increase in data points that Rainflow must analyze. An increase in data points results in more frequent updates to the crack size estimate. Every additional update to crack size will consume additional computation time. Therefore, the number of computations possible per buffer will decrease due to the increase in computation time.

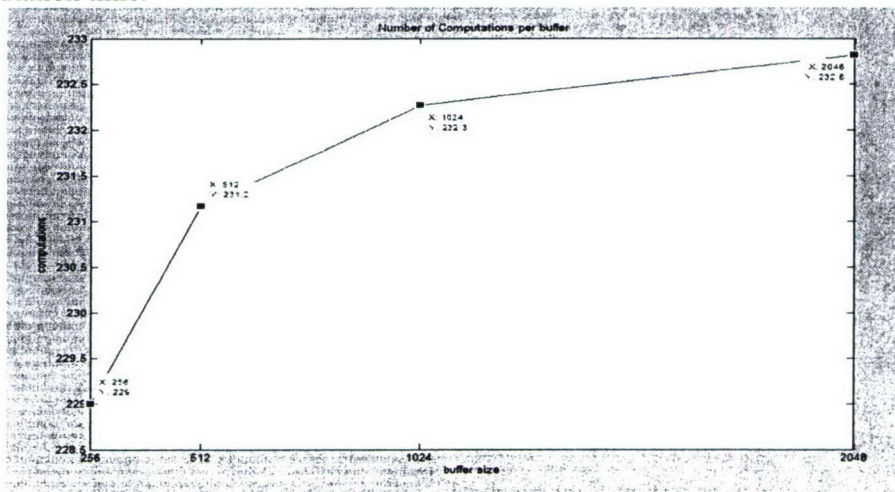


**Figure 2.50 Computation vs. buffer size**



### 2.6.3 Sample Rate Performance Analysis

Buffer sizes of 256, 512, 1024, and 2048 were evaluated to determine the maximum sample rate.

```
buff = [256,512,1024,2048]    // buffer sizes
clk = 225e6                    // clk speed (Hz)
Tclk = 1 / clk                  // clk period (s)
```

$$C = [(mod\ 1 + mod\ 2 + \dots + mod\ M) * buffSize] + (subf_1) * 5 + (subf_2) * 10 + \dots subf_N * X_{max}$$

C represents cycles needed to process a buffer of data. To calculate the best sample rate possible the cycles needed to compute a buffer of data are multiplied by the cycle period. To obtain a per-input sample rate, this buffer sample rate is divided by the size of the respective buffer.

```
Tb = C * Tclk                // max buffer sample rate (s)
Tmax = Tb / buff              // max sample rate achievable (s)
```

The subf1 and subf2 sub-functions are only executed upon the calculation of an output. Since an output is not always computed for every input, the algorithm exhibits non-linear behavior. The constant multipliers of 5 and 10 are derived from observing that, for a given buffer of flight data, subf1 and subf2 were, at most, calculated 5 and 10 times, respectively. Since no two flights will record the same input data, these multipliers may not be the same. This will change the ideal sample rate from flight to flight. Therefore, the ideal sample rate should be derived from data representing a worst case scenario. In this case, a flight with high engine stresses. A worst case sample rate (lowest sample period) can be determined by benchmarking the implementation with data sets from different flight missions. The implementation achieves a maximum sample rate of 2.14 us when using a buffer of 2048 floating point values as seen in Table 2.6.

**Table 2.6 Maximum input sample rate**

Max data sample rate (us)			
256	512	1024	2048
2.17	2.15	2.14	2.14

### References

- [1] M. Matsuiski, and T. Endo, "Fatigue of metals subjected to varying stress", Japan Soc. Mech. Engrg., 1969.
- [2] S.D. Downing, and D.F. Socie, "Simplified rainflow counting algorithm", Int. J. of Fatigue, Vol. 4, No. 1, pp. 31-40, 1982.



- [3] C. Amzallag, J.P. Gerey, J.L. Robert and J. Bahuaudt, "Standardization of the rainflow counting method for fatigue analysis", *Int. J. Fatigue*, Vol. 16, pp. 287, 1994.
- [4] ASTM E1049-85, "Standard practices for cycle counting in fatigue analysis", pp. 789-797, Reapproved 1990
- [5] G.R. Leverant, H.R. Millwater, R.C. McClung, M.P. Enright, "A new tool for design and certification of aircraft turbine rotors," *Journal of Engineering for Gas Turbines and Power*, Vol. 126, No. 1, pp. 155-159, 2004
- [6] H.R. Millwater, P.H. Wirsching, "Analysis method for probabilistic life assessment"
- [7] B.W. Silverman, "Density estimation for statistics and data analysis", pp. 43.
- [8] A.H. Ang, W.H. Tang, "Probability concepts in engineering planning and design", Vol. 1, pp. 329-344.

### **3. DURABILITY OF SENSING MATERIALS**

#### **3.1 Background & Objectives**

Vehicle health management (VHM) requires on-board sensors that are typically actuated using materials that exhibit shape memory, piezoelectric, or magnetostrictive behavior. In many cases, these sensing materials are used in the form of multi-layered structures whose functionalities and performance characteristics are intimately linked to their nanocrystalline or amorphous states. Furthermore, the durability and functionalities of thin-film materials are known to depend on layer thickness and likely on test temperature. Unfortunately, these material properties are generally not available for thin-film materials. Since on-board sensing devices must be more durable than the components that are being monitored, there is a strong need determine the operative damage mechanism and to characterize the durability of thin-film sensing materials in the pertinent size scale and under conditions that are relevant to the service environment, which usually involves fatigue or thermomechanical loading. The initial focus of this effort will be on magnetostrictive thin film sensor materials because of the anticipated importance to VHM and relative lack of durability information.

The objectives of this task are: (1) to determine the durability of magnetostrictive sensing materials subjected to mechanical, electrical, and thermal loading, (2) to evaluate the dependence of the performance and durability on layer thickness, and service temperature, and (3) to develop a durability model to optimize sensor durability with respect to layer thickness and compliant layer. The first year of this program is focused on a room temperature assessment, while elevated temperature assessments are planned for years two and three.

### 3.2 First Quarter Accomplishment

An integrated experimental/nanomechanical modeling approach is being utilized. Innovative processing techniques are being used to deposit thin-film layered sensor materials on an engineering alloy substrate using processing parameters developed on a parallel DARPA-sponsored program. Novel experimental techniques will subsequently be employed to characterize the microstructure, yield strength, fatigue, and sensing (i.e., piezoelectric or magnetostrictive) properties of the thin-film sensor materials. These include nano-indentation to characterize the elastic modulus, yield strength, fracture toughness, and interface toughness of selected thin films as well as SEM, TEM, AFM, and optical microscopy to identify the failure mechanisms. The effects of layer thickness and temperature on the mechanical and functional properties will be interrogated and correlated to the underlying nanocrystalline or amorphous state in order to identify the pertinent failure mechanisms. A fundamental understanding of the relationships between bond coat, layer thickness, and temperature on the durability and functionalities of thin-film sensor materials will be developed by modeling the failure process at the nanoscale level. The initial low temperature results would be applicable to fan and compressor applications, whereas the elevated temperature results proposed in the later years of the program would be applicable to turbine discs.

During this reporting period, efforts were initiated to develop experimental techniques for characterizing thin-film sensor materials. Three thin-film magnetorestrictive sensor specimens were provided by Dr. Bruce Lanning at SwRI. Generated as part of the DARPA Material Prognosis Program, these thin-film sensor specimens included the following:

Sample 1: 2  $\mu\text{m}$  Fe-Co thin-film on a Si substrate

Sample 2: 7  $\mu\text{m}$  Fe-Co thin-film on a Si substrate

Sample 3: 1  $\mu\text{m}$  Fe-Co with a Cu compliant layer on a Ti-6Al-4V substrate

All films were fabricated by physical vapor deposition.

The integrity of the as-deposited thin-films was characterized by performing nanoindentation tests and micro-scratch tests. The former was utilized to determine the elastic modulus and hardness of the thin-film sensor materials, while the latter was utilized to evaluate the bond strength and fracture toughness of the thin-film/substrate interface. These tests were performed using an MTS nanoindentation test system (NanoIndenter® XP) at MTS, Oak Ridge, TN. We are currently in the process of purchasing such a test system for use in this project.

The nanohardness tests were performed using a Berkovich indenter with MTS' patented Continuous Stiffness Measurement (CSM) technique. With this technique, a small oscillation was superimposed on the primary loading signal and the resulting response of the system was analyzed by means of a frequency-specific amplifier. The excitation frequency was held constant throughout the test at 45 Hz. The excitation amplitude was controlled such that the resulting displacement amplitude remains constant at 2 nm. An array of 10 indents was performed on each sample; successive indents are separated by approximately 75 microns. With the CSM technique, each



indentation experiment allows a continuous measure of the contact stiffness,  $S$ . Using the dynamic measure of  $S$ , and established formulae for elastic modulus and hardness, every individual indentation experiment yielded elastic modulus and hardness as a continuous function of surface penetration. The results for elastic modulus and hardness vs. penetration for the ten indentation experiments on a particular sample were averaged using discrete displacement windows of approximately 5 nm. Using the data in each window, an average and standard deviation were calculated. Figure 3.1 presents preliminary results of the elastic moduli of the thin-film specimens as a function of penetration depth into the thin film. The low elastic modulus of Sample 3 likely reflects the thinness of the Fe-Co film, combined with the presence of the Cu compliant layer.

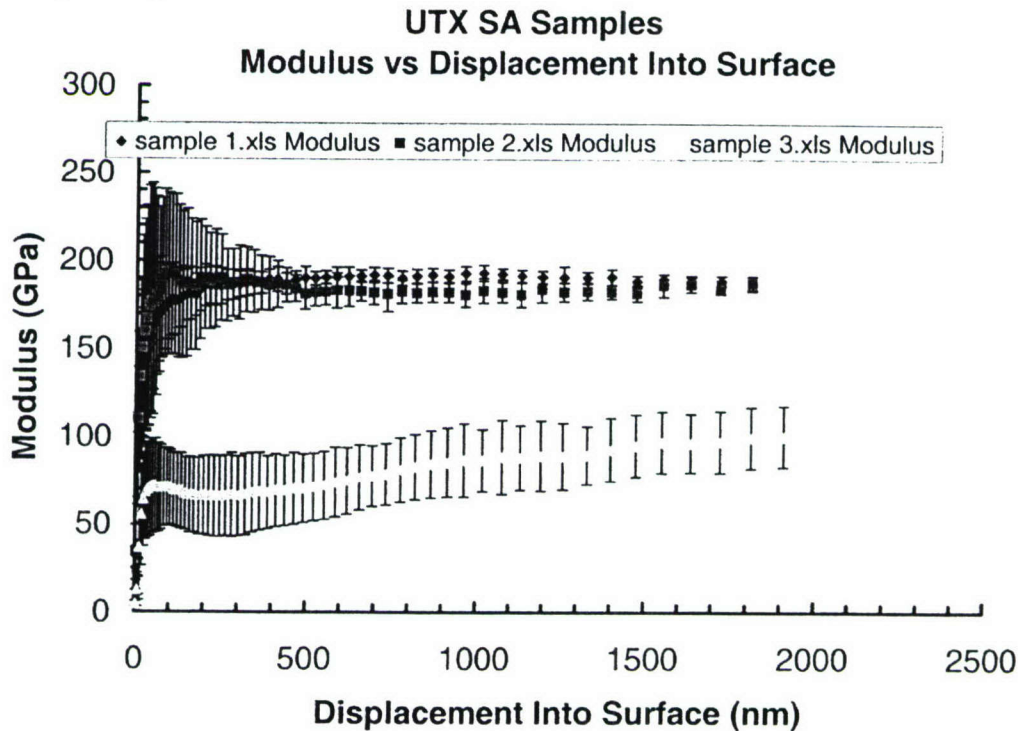


**Figure 3.1.** Elastic moduli of thin-film sensor materials as a function of indent penetration into the thin film surface.

Microscratch tests were also performed on individual thin-film specimens via the MTS nanoindenter. During the scratch tests, load-displacement curves were obtained for both axial and lateral directions. We are currently in the process of analyzing these results.

### 3.3 Second Quarter Accomplishment

Load-displacement curves of microscratch tests performed on individual thin-film specimens via the MTS nanoindenter were analyzed. During the scratch tests, load-displacement curves were obtained for both axial and lateral directions. A drastic change in the load-displacement response occurred when the thin film



debonded from the substrate. Thus, the microscratch test appears to be a useful test for determining the debonding strength for toughness for thin film sensors. However, more work is required to identify the onset of debonding from the load-displacement curve.

The composition of the thin film material was chosen to be  $\text{Fe}_{50}\text{Co}_{50}$  with possible additions of V. The film thickness chosen for studies were 1 and 5  $\mu\text{m}$  either with or without a compliant layer. The dimensions of the thin film sensors are  $0.25'' \times 1''$ . Two different compliant layers are planned, but the materials have not been selected at this time.

A test matrix was developed for assessing the durability of the thin film material bonded on a Ti-6Al-4V substrate. The test matrix was designed on the basis of the expected fatigue life of Ti-6Al-4V at ambient temperature and at a stress ratio, R, of 0.1, as shown in Table 1. Since a disk is generally designed to a low-cycle fatigue (LCF) life of 50 to 100 kilocycles, a stress range ( $\Delta\sigma$ ) of 100 ksi was selected for fatigue testing of thin film sensor material according to the test matrix shown in Table 2. Triplicate tests are planned for Ti-6Al-4V with two thicknesses of  $\text{Fe}_{50}\text{Co}_{50}$  with or with a compliant layer. As shown in Table 2, a total of 25 test specimens are to be fabricated, 15 tests are planned with 10 tests (spares) to be determined at a later date.

Table 1. Predicted Stress-Life Behavior for Ti-6Al-4V at Various Maximum Stress ( $\sigma_{\text{max}}$ ) or Stress Ranges ( $\Delta\sigma$ )

$\sigma_{\text{max}}$ [ksi]	$\Delta\sigma$ [ksi]	R-ratio	Expected Life
110	100	0.1	~15,000
100	90	0.1	60,000-100,000
95	85.5	0.1	100,000+

Table 2. Test Matrix for Durability Studies of  $\text{Fe}_{50}\text{Co}_{50}$  Thin Film Bounded to Ti-6Al-4V

$\Delta\sigma$ [ksi]	Without Film	With Film, but no CL		With Film + CL	
		1 $\mu\text{m}$	5 $\mu\text{m}$	CL1	CL2
100	XXX	XXX	XXX	XXX	XXX

Specimens: 25

CL = Compliant Layer

Planned Tests: 15

Spares: 10 (for additional replication or exploration of additional film thicknesses or compliant layers)

The test specimen is in the form of a thin strip with the dimensions shown in Figure 3.2. Three-point bending will be used for the fatigue tests. A schematic of the three-point bend fatigue test set-up is shown in Figure 3.3. Also shown in Figure 3.3 are five locations where thin film sensors ( $0.25'' \times 1''$ ) will be placed to assess the

durability of the thin film sensors. Three sensors will be placed at different stress levels near the center of the tension side of three-point bend specimen. Two sensors will be placed at the free ends under zero stress on the compression side of the test specimen. These two sensors will be used to detect possible crack initiation in the sensors and the substrate at various stressed locations in the center of the three-point bend specimens. The performance of the sensors will be monitored both under active and passive modes as a function of fatigue cycles.

Machining of the Ti-6Al-4V test specimens are currently underway. An existing test fixture is available for the three-point bend fatigue tests, but a few rollers of the desired dimensions need to be fabricated. Fabrication of the rollers is also underway. Both the specimens and the test fixture are expected to be ready for deposition of thin film to commence in January 2005, followed by fatigue testing.

Theoretical modeling of the durability of thin film sensor materials was initiated. The modeling efforts were focused on addressing two issues: (1) the changes in the fatigue resistance of the substrate due to the presence of surface-bonded thin film sensors, and (2) the resistance to fatigue crack initiation and growth in the thin-film sensor materials. To address the first issue, modeling effort was initiated in the reporting period to examine how a thin film sensor can alter the fatigue crack initiation and growth lives of the substrate. The modeling effort will continue in the next reporting period and will involve the use of a physics-based fatigue crack initiation and growth model developed under AFOSR MEANS program [1] to predict fatigue crack initiation and growth lives of the substrate without and without the thin film sensor. In the latter case, the thickness of the thin film materials and the nature of residual stresses in the material will also be considered. Theoretical modeling to address the second issue will commence after the durability tests of the thin film material are underway.

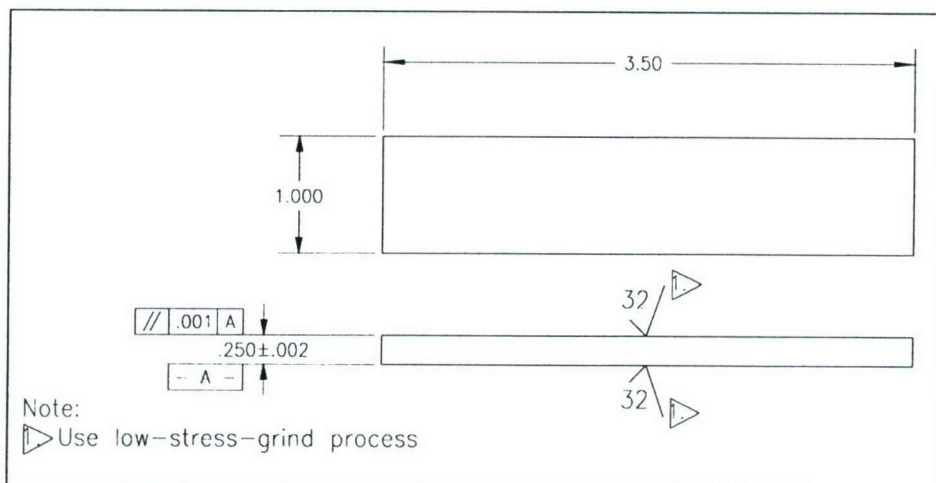


**Figure 3.2.** Proposed specimen geometry and dimensions (in inches) for three-point bend fatigue testing of  $\text{Fe}_{50}\text{Co}_{50}$  thin film bonded to a Ti-6Al-4V substrate. Specimen is shown without the thin film materials.



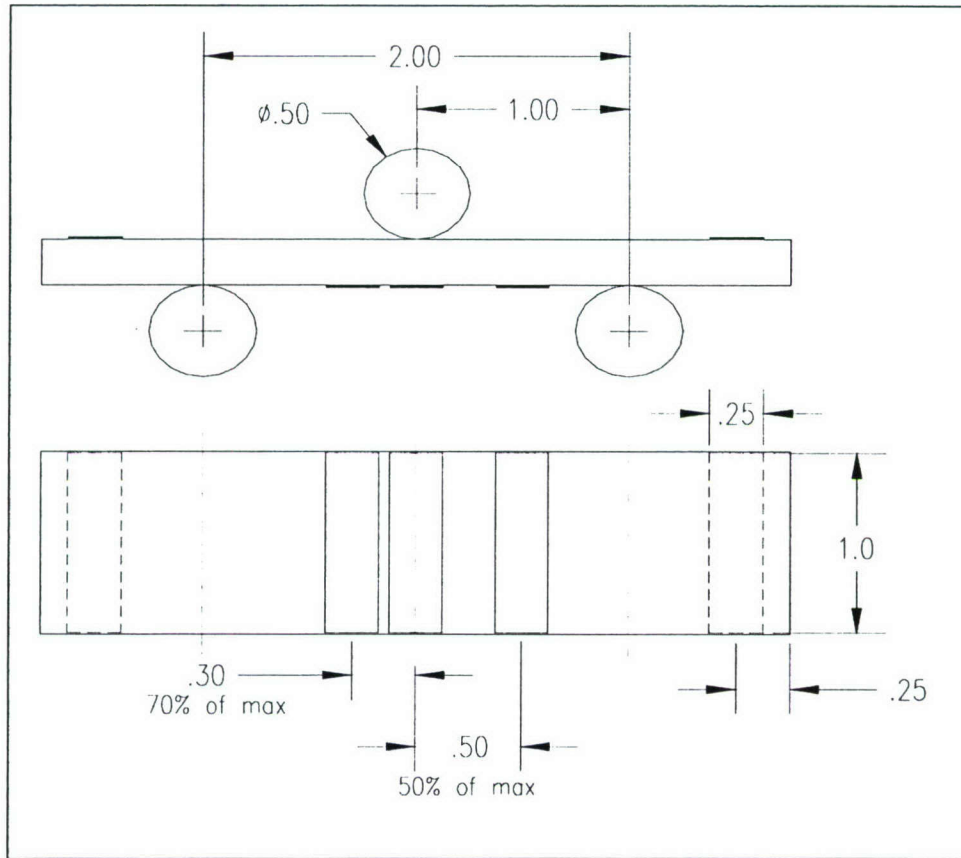


**Figure 3.3. Specimen loading geometry and approximate sensor dimensions and locations. The thin film sensors are 0.25" × 1" and are schematically shown as rectangular boxes of either solid lines or dashed lines. All dimensions are in inches.**

### 3.4 Third Quarter Accomplishment

During this quarter, Fe-Co thin-film microstructures and properties were characterized, and initial fatigue tests with these films deposited on a Ti-6Al-4V alloy typical of fan and compressor components in turbine engines were performed. Predictions from micromechanical fatigue models were compared with the measured data. This comparison, combined with an initial assessment of the failure mode of the films, suggests that the film durability can be enhanced by improving the decohesion strength of the film-to-substrate interface. Methods to improve the interfacial decohesion have been identified and will be pursued during the next quarter.

### 3.5 Final Accomplishment

Significant progress was made to assess the durability of FeCo thin films bonded to Ti-6Al-4V in the last reporting period, which included: (1) measuring the interface toughness, (2) determining the debonding stresses, (3) identifying fracture mechanisms, and (4) characterizing the fatigue life response of FeCo/Ti-6Al-4V. Detailed



descriptions of these findings are presented in a recent paper [1]. Key findings in this investigation are highlighted in the next four subsections.

### 3.5.1 Interface Fracture in FeCo/Ti-6Al-4V

Indentation interface fracture toughness tests were performed at ambient temperature using a brale 'C' indenter (120° diamond cone with a slightly rounded point) in a Rockwell hardness tester. The brale indenter was pushed into the FeCo thin film and the Ti-6Al-4V substrate under a constant applied load. After indentation, the diameter of the indent, the size of the debonded region and the cracked region on the thin film were measured by optical microscopy (OM) and scanning electron microscopy (SEM). The sizes of the indented and the cracked region, as well as the residual stresses in the thin film, which were determined separately by curvature measurements of the thin film deposited on Kapton, were then utilized as input to the interface fracture model developed by Drory and Hutchinson [2] to compute the elastic strain energy release rate ( $G_i$ ) at interface fracture for FeCo thin films bonded to Ti-6Al-4V.

Figures 3.4(a) and (b) show the optical and secondary electron images of brale indents on FeCo/Ti-6-4 and the corresponding debonded and cracked regions in the thin film, respectively. For both cases, the largest diameter was taken to be the size of the debonded or the cracked region. A direct comparison of the interface toughness using the debonded region determined by OM and the cracked region determined by SEM indicated that the diameter of the cracked region provided interface toughness values that were more reasonable than those obtained using the diameter of the debonded region measured by OM. Thus, all interface toughness values were determined on the basis of the maximum diameter of the cracked region measured by SEM, assuming the debonded region extended as far as the cracked region. Figure 3.4(b) shows that cracks in the FeCo thin films are debonded from the substrate.

Figure 3.5(a) presents the results of the interface toughness of a single 4  $\mu\text{m}$  thick FeCo thin film on Ti-6Al-4V determined at various applied loads. In a second set of experiments, the applied load was fixed at 15 kg, but the location was varied for indentation measurements along the length (25.4 mm) of the 4  $\mu\text{m}$  thin film, Figure 3.5(b). As shown in Figure 3.5(a), most of the interface toughness values ( $G_i$ ) obtained from the first set of experiments were in the range of 2 – 4  $\text{J/m}^2$ , but occasionally showed higher values (6 – 8  $\text{J/m}^2$ ) at higher indentation loads (60 – 100 kg). In comparison, the interface toughness obtained by varying the indentation location at a constant load (15 kg) showed an interface toughness value of  $7.03 \pm 2.41 \text{ J/m}^2$  compared to  $4.45 \pm 1.74 \text{ J/m}^2$  for those of 30 - 100 kg loads, Figure 2(b). Thus, the interface toughness due to spatial variation was larger than that exhibited by indentation load variation. Since the interface toughness value was similar for most indentation loads, it was thought that the variations at some indentation loads were the result of toughness variation with the indentation location and not the effect of the indentation load.

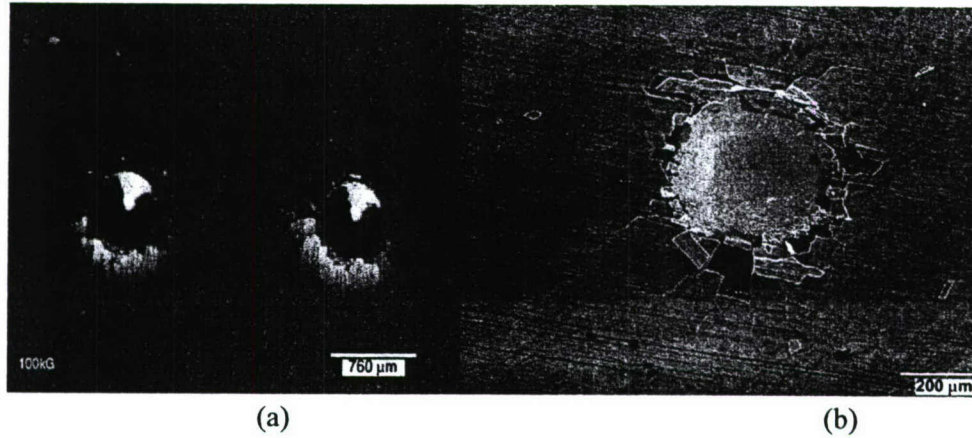


**Figure 3.4.** Optical and SEM images of a brale indent on FeCo/Ti-6Al-4V showing debonded and cracked ones in the indented thin film: (a) optical image taken with side lighting, and (b) SEM image.

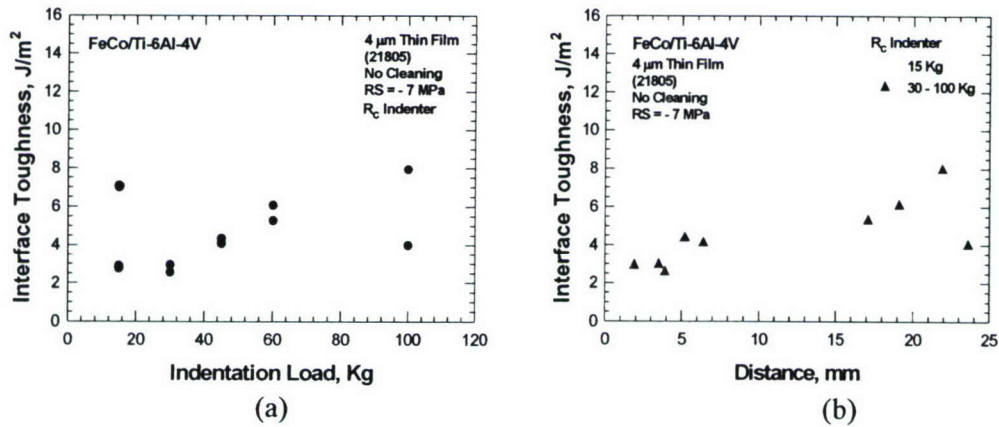


**Figure 3.5.** Interface toughness of a 4 μm FeCo thin film measured using a brale indenter in a Rockwell hardness tester: (a) as a function of indentation load, and (b) as a function of location.

In addition to 4 μm thick films, the interface toughness values of three FeCo thin films along the length of the films were also measured for film thickness of 4.56, 3.27, and 0.9 μm. For these three cases, the interface toughness varies with location and ranges from the lowest at 1.9 J/m<sup>2</sup> to the highest at 5.9 J/m<sup>2</sup>. The locations of the lowest and highest values of the interface toughness are different in the thin films examined. On the other hand, the mean and the standard deviations do not show large variations with film thickness, as shown in Figure 3 which presents the interface toughness as a function of film thickness. The results indicate that the average value of the interface toughness is approximately the same ( $\approx 4$  J/m<sup>2</sup>) with a standard deviation in the range of  $\pm 1 - 1.8$  J/m<sup>2</sup>, Table 1. The corresponding coefficient of variation (COV) ranges from 23.8% to 41.8%. Neither the mean nor the coefficient of variation shows an obvious dependence on the film thickness for the range of thickness (1–5 μm) examined. Thus, it is concluded that for the FeCo thin films examined, the interface toughness is independent of the film thickness.



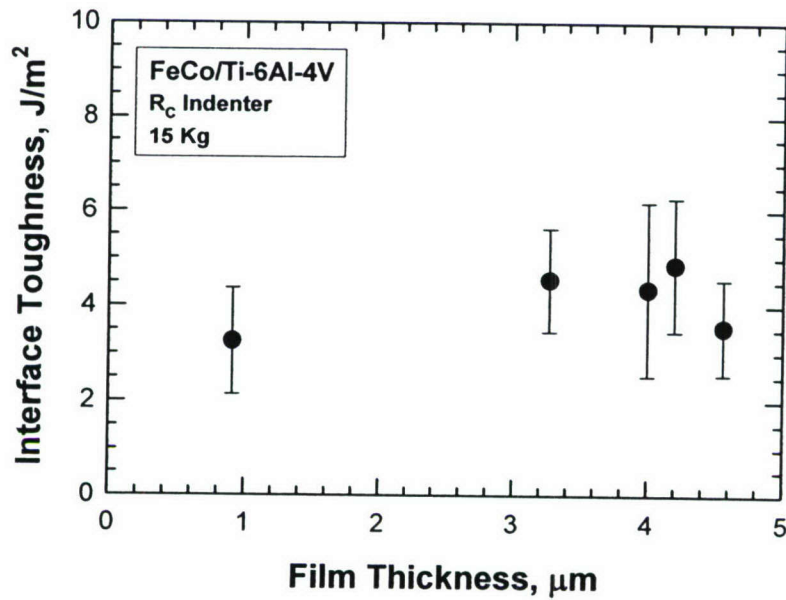


**Figure 3.6. Interface toughness of FeCo thin films as a function of film thickness.**

**Table 1.** Interface Toughness ( $G_i$ ) and Debonding Stress ( $\sigma_d$ ) of FeCo Thin Films on Ti-6Al-4V Compared Against Fatigue Lives of Ti-6Al-4V with and without FeCo Thin Films Tested at a Maximum Stress of 758 MPa and at  $R = 0.1$ . Standard Deviations Based on Three Tests or More are Shown in Parentheses.

Film Thickness, $\mu\text{m}$	$G_i$ , $\text{J/m}^2$	$\sigma_d$ , MPa	Fatigue Life, Cycles
0.9	3.25 (1.12)	> 758	74,646 (7156)
3.27	4.53 (1.08)	> 758	—
3.8	—	668.8	—
4.0	4.36 (1.82)	533.4 (65.2) 500.7 (44.5)	60,239 (4450)
4.2	—	587.2 (46.9)	—
4.56	3.56 (1.0)	323.0 (58.9)	—
6.8	—	432.5 (86.8)	—
7.5	—	305.7 (133.3)	57,380 (2460)
Without thin film	—	—	62,894 (3680)

Nanoindentation tests were performed at UTSA to characterize the elastic modulus, hardness, and yield strength of FeCo thin films on Ti-6Al-4V for two different film thickness and surface conditions. The nanoindentation tests were carried out using the continuous stiffness measurement technique of MTS with a Berkovich indenter. An array of five indents was performed on each specimen and the results are summarized



in Table 2. In addition, a cross-sectional nanoindentation technique, which involved indenting on the edge of a coated specimen to cause debonding of the thin film from the substrate, was utilized to measure the interface toughness on the basis of the load-displacement curve, the size of the indent, and the interface crack length. Preliminary results, shown in Table 2, indicate that the interface toughness for a 4  $\mu\text{m}$  thin film deposited on a polished Ti-6Al-4V surface are about 2.1 to 3.7  $\text{J/m}^2$ , which are in agreement with those obtained using the brale indentation technique. Cross-sectional indentation tests for the 1  $\mu\text{m}$  film and other surfaces are in progress.

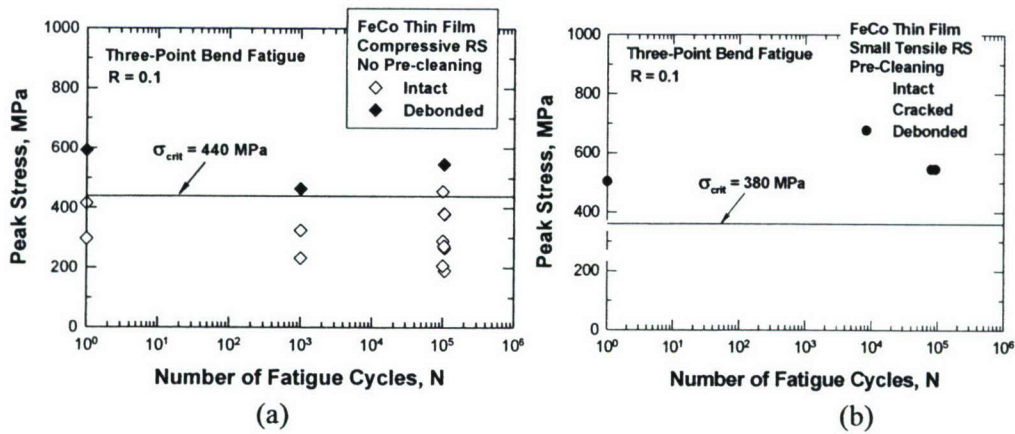
Table 2. A Summary of Young's Modulus, Hardness, and Yield Strength, and of FeCo Thin Films Determined by Nanoindentation Together with Interface Toughness ( $G_i$ ) Determined by Cross-sectional Nanoindentation

Test Sample	Young's Modulus of Film (GPa)	Hardness of Film (GPa)	Yield Strength of Film (MPa)	$G_i$ , $\text{J/m}^2$
4.1 $\mu\text{m}$ FeCo Film on polished Ti-6-4	167.7	10.7	3570	$2.08 \pm 1.57$ $3.73 \pm 2.1$
4.1 $\mu\text{m}$ FeCo Film on unpolished Ti-6-4	164.8	10.4	3470	In Progress
0.9 $\mu\text{m}$ FeCo Film on polished Ti-6-4	201.4	8.5	2830	In Progress
0.9 $\mu\text{m}$ FeCo Film on unpolished Ti-6-4	206.1	8.7	2900	In Progress

### 3.5.2 Debonding Stress for FeCo/Ti-6Al-4V

The critical stress at the onset of interface decohesion in FeCo/Ti-6Al-4V was determined as a function of thin film thickness by monotonic loading via three-point bending. The interface debonding stresses by three-point bending are summarized in Table 1 together with the interface toughness determined by indentation. As shown in Table 1, FeCo thin films with thickness greater than 4  $\mu\text{m}$  debonded at stresses below 600 MPa. The debonding stress decreases with increasing film thickness. In comparison, FeCo thin films with thickness in the 1 – 3  $\mu\text{m}$  range remained intact and did not debond at a tensile stress as high as 758 MPa, implying that the debonding stress was greater than 758 MPa for the FeCo films with a thickness of 1 – 3  $\mu\text{m}$ .

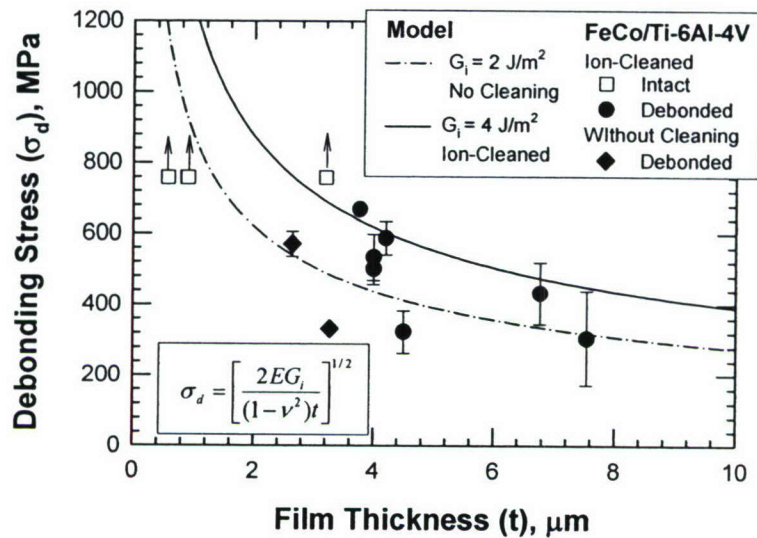
In addition to film thickness, the debonding stress of FeCo thin film was also determined as a function of fatigue cycles. Figure 3.7(a) and (b) summarize the conditions of the thin film for various peak stresses and fatigue cycles for 4  $\mu\text{m}$  thin films with tensile and compressive residual stresses, respectively. In Figure 3.7(a), the FeCo thin film remained intact at stresses below 440 MPa, but debonded at stresses above 440-460 MPa. In Figure 3.7(b), the thin film was intact at stresses below 380 MPa, but started to form cracks at stresses above 380 MPa and become debonded at stresses above 500 MPa. For both cases, the debonding stresses were essentially independent of the number of fatigue cycles. On the other hand, the thin film with a compressive residual stress exhibited a somewhat higher debonding stress (440 MPa, Figure 3.7(a)) than the one with a tensile residual stress (380 MPa, Figure 3.7(b)).



**Figure 3.7. Debonding stress values of 4 $\mu$ m thick FeCo thin films bonded to Ti-6Al-4V substrate as a function of the number of fatigue cycles: (a) with compressive residual stresses and no surface pre-cleaning, and (b) with tensile residual stresses and surface pre-cleaning.**

A summary of the debonding stresses for FeCo thin films on Ti-6Al-4V is presented as a function of thin thickness in Figure 3.8, which indicates that the debonding stress increases with decreasing FeCo thickness for thickness less than 4  $\mu$ m. For film thickness less than 3  $\mu$ m, the thin films did not debond at 748 MPa. For thin films deposited on surfaces without ion-cleaning, the interface toughness was about 2 J/m<sup>2</sup>, while  $G_i$  was about 4 J/m<sup>2</sup> for thin films deposited on ion-cleaned surfaces. The corresponding debonding stresses computed based on a critical energy release rate are in reasonable agreement with the experimental data, as shown in Figure 3.8. The lower interface toughness (2 J/m<sup>2</sup>) gives debonding stresses that are comparable to the lower bound data of the thicker thin films (> 4.2  $\mu$ m), while the higher interface toughness (4 J/m<sup>2</sup>) gives debonding stresses that are comparable to the upper bound data of the thin films over the entire range of film thickness investigated. The results in Figure 3.8. suggest that interface debonding in FeCo/Ti-6Al-4V is governed by a critical elastic energy release rate. The debonding stress is seen to increase with decreasing film thickness. A large variability exists in the experimental values of the debonding stress for FeCo/Ti-6Al-4V because the interface toughness varies with location and shows a substantial scatter (25 – 40% COV). In general, there is a tendency for decohesion to occur at the location where the interface toughness is lowest assuming the local stresses in the neighboring surround are approximately equal. As a result, the observed debonding stress values often fall below those predicted on the basis of the average values of the interface toughness, as shown in Figure 3.8.

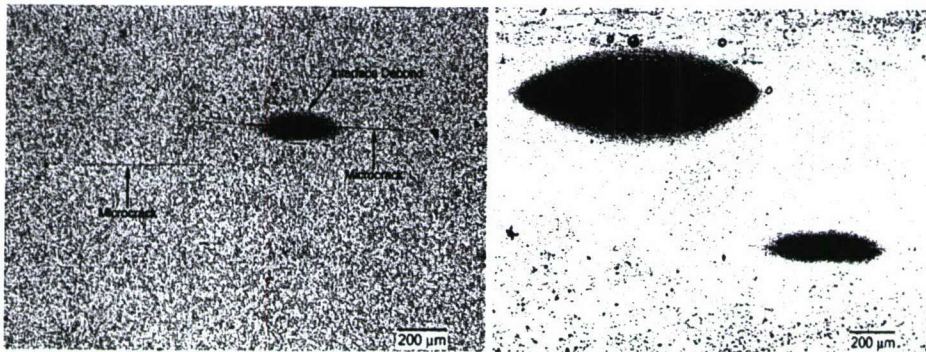




**Figure 3.8.** A comparison of the measured and predicted debonding stresses for FeCo thin films on Ti-6Al-4V shows that the debonding stress in FeCo thin film increases with decreasing film thickness according to a critical elastic energy release rate criterion. Ion-cleaning increased the interface toughness from 2 J/m<sup>2</sup> to 4 J/m<sup>2</sup> and increased the debonding stress.

### 3.5.3 Fracture Mechanisms

For both monotonic and cyclic loading, the debonding process appeared to be driven by the peak stress. The sequence of events involved in the film decohesion process that have been identified from several interrupted monotonic and cyclic tests. The first step of the decohesion process in FeCo/Ti-6Al-4V was the formation of a crack in the FeCo thin film, Figure 3.9(a). Once a crack was present in the thin film, the thin film adjoining the crack became debonded. The debonded regions reflected light differently and appeared dark in the optical micrograph shown in Figure 3.9 (b). Continued cyclic loading caused the both the film crack and the debonded interface to grow with increasing stresses or the number of fatigue cycles, eventually leading to detachment of patches of the thin film from the substrate, as shown in Figure 3.9 (c). In all cases, cracks in FeCo resulted in film detachment without propagating into the Ti-6Al-4V substrate.





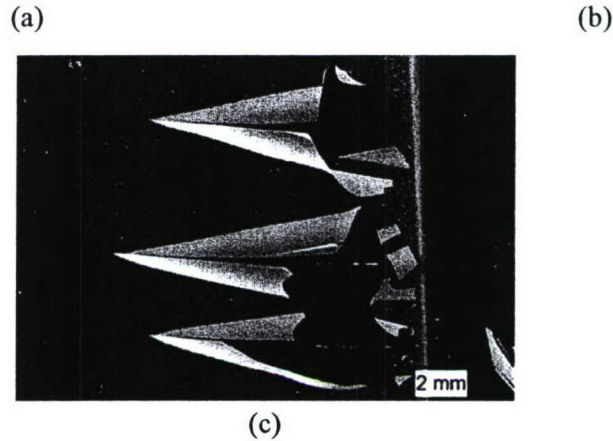


**Figure 3.9. Fracture mechanisms observed in FeCo/Ti-6Al-4V subjected to three-point-bend fatigue at a stress ratio,  $R$ , of 0.1: (a) microcracks in the FeCo thin film, (b) interface debonds (dark areas) in FeCo/Ti-6-4 and the cooperative growth of microcracks and interface-debonds with fatigue cycling, and (c) debonded patches on FeCo thin film.**

The fracture mechanics of crack deflection versus crack penetration has been analyzed by He et al. [3] who presented the result in terms of a plot of  $G_i/G_p$  as a function of the Dundurs parameter [4],  $\alpha = (E_1 - E_2)/(E_1 + E_2)$  [3], where  $G_i$  is the interface toughness or the critical energy release of the interface crack and  $G_p$  is the critical energy release rate for crack penetration into the substrate;  $E_1$  and  $E_2$  are the Young's moduli of the thin film ( $E_1 = 1.7 \times 10^5$  MPa) and substrate ( $E_2 = 1.7 \times 10^5$  MPa), respectively. The theoretical crack morphology transition boundary is shown in Figure 3.10 as the solid curve. Crack penetration into the substrate occurs for  $G_i/G_p$  ratios above the solid curve, while interface cracks remain to propagate along an interface for  $G_i/G_p$  values that are less than the solid boundary. One possible measure of the  $G_p$  is the fracture toughness of the substrate. For Ti-6Al-4V,  $K_{IC}$  is at least 67 MPa/m [5]. This leads to a  $G_p$  in excess of  $2.4 \times 10^4$  J/m<sup>2</sup>. The value of  $G_i$  range from 2 – 4 J/m<sup>2</sup> for FeCo/Ti-6Al-4V. The corresponding  $G_i/G_p$  ratio is  $8E-5$  to  $1.6E-4$ , which are shown as filled circles in Figure 3.10. Another possible measure of  $G_p$  is the fatigue crack growth threshold,  $\Delta K_{th}$ , of small cracks or large cracks at a high  $R$  ratio. For Ti-6-4,  $\Delta K_{th} = 2$  MPa/m [5] and it leads to  $G_p = 21$  J/m<sup>2</sup> and a  $G_i/G_p$  ratio of 0.095 - 0.19, which are shown as filled squares in Figure 3.10. For both measures, the ratios of  $G_i/G_p$  ratios are below the boundary for crack penetration into the substrate. Thus, the interface cracks are expected to propagate along the interface and would not penetrate into the substrate. On the other hand, the  $G_i/G_p$  ratio for a fatigue crack is 0.19, which is not too far the critical value of 0.25 required for crack penetration to occur. An interface toughness in excess of 5.25 J/m<sup>2</sup> would move the  $G_i/G_p$  ratio on or above the transition boundary. Thus, the interface toughness of FeCo thin films are currently optimized for interface fracture without fatigue crack penetration into the Ti-alloy substrate. The finding is supported by experimental observations, shown in Figure 3.9(c), which indicates that the interface cracks propagated across the entire width and length of the FeCo thin film without penetrating into the substrate. In many instances, small patches of the debonded thin films peeled away from the substrate while still attached to the surface. In others

cases, the patches became detached from the specimens leaving an opening on the thin film.

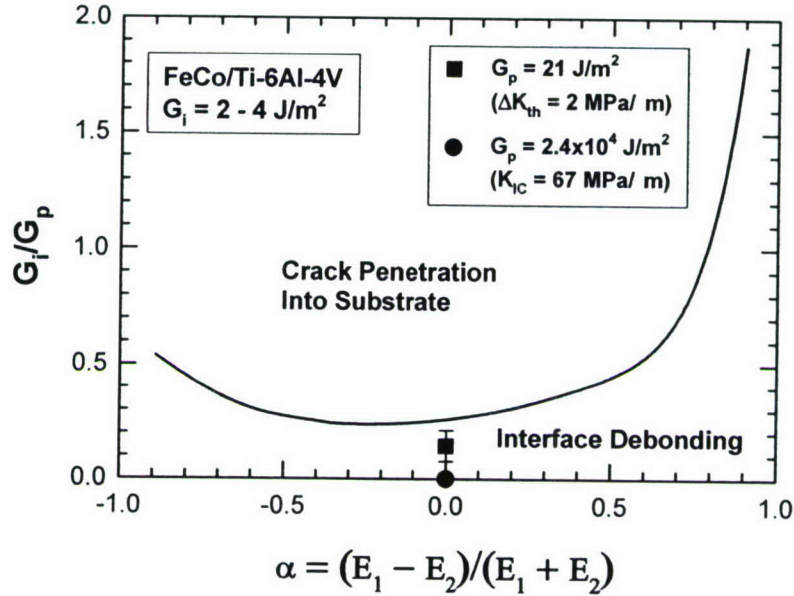


**Figure 3.10.** Plot of  $G_i/G_p$  ratio as function of the Dundurs parameter  $\alpha$  [4] shows the interface toughness,  $G_i$ , of FeCo thin films is small compared to the critical energy rate for crack penetration,  $G_p$ , into Ti-6Al-4V such that the  $G_i/G_p$  ratios reside in the region characterized by interface debonding exclusively and is far from the theoretical boundary [3] for transitioning to crack penetrating into the substrate.

### 3.5.4 Fatigue Life Response

The effects of FeCo thin films on the low-cycle fatigue life ( $10^4 - 10^5$  cycles) response of Ti-6Al-4V were investigated by performing three-point bend fatigue of rectangular plates with and without thin films at a peak stress of 748 MPa and  $R = 0.1$  until fracture. Table 1 summarized the fatigue lives for specimens with and without thin films. For uncoated specimens, the fatigue life was 62.9 kcycles, compared to 74.6, 66, and 57.4 kcycle for 1, 4, and 7.5  $\mu\text{m}$  film thickness, respectively. The results indicate that the fatigue life of Ti-6Al-4V with thin films is essentially identical to those without thin films. For the coated specimens, the thin films appeared to have a small effect on the fatigue life, with increasing fatigue life with decreasing film thickness. Examination of the fatigue surfaces revealed that fatigue cracks initiated at the edge of the bend specimens for both coated and uncoated specimens with similar fracture surfaces. In all four cases, fatigue cracks initiated at the corner edge of the specimens, but the grain where the fatigue crack first appeared was not identified because of the absence of any identifiable markings or discernable features. For the coated specimens, fatigue cracks initiated on the side edges of the specimens and was not located at or beneath the FeCo thin film. Thus, fatigue crack initiation in the FeCo-coated specimens could not be attributed to the FeCo thin films. The similarity of the fatigue surfaces suggests that fatigue cracks initiated in the Ti-6Al-4V substrate



for both coated and uncoated materials, which explains the similarity in the observed fatigue lives.

The fatigue life of the Ti-6Al-4V plate was previously characterized by axial fatigue of rounded bars as part of the AFRL High Cycle Fatigue (HCF) Program [6]. The fatigue life results from this study are compared against those for the HCF program in Figure 3.11, which shows the three-point bend fatigue data from this study exhibited slightly longer life than the axial fatigue life data from the HCF program. The difference in the bending and axial fatigue lives is attributed to the stress gradient associated with three-point bend fatigue and not from the presence of thin films on the bend specimens.

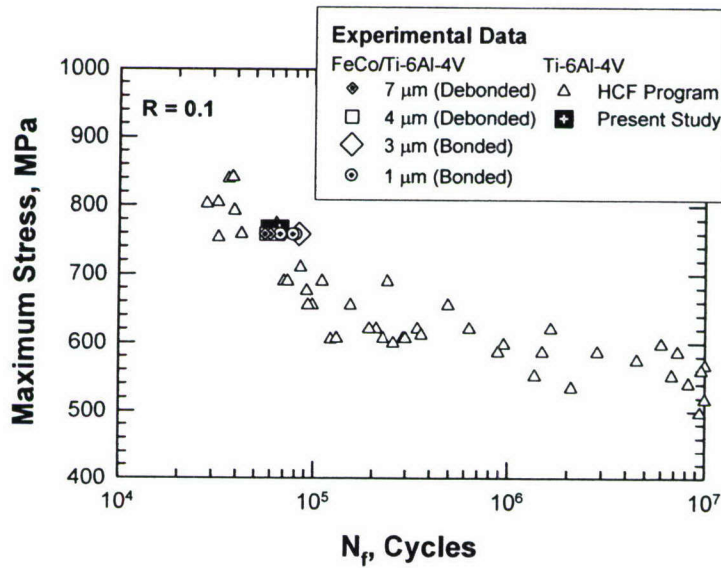


**Figure 3.11. Fatigue life of three-point-bend fatigue of Ti-6Al-4V with and without FeCo thin film compared to those of axial fatigue generated in the Air Force HCF Program [6].**

### 3.5.5 Conclusions

The conclusions reached in this investigation are as follows:

1. The debonding stress of FeCo thin films on Ti-6Al-4V increases with decreasing film thickness according to a critical energy release rate.
2. The interface toughness of FeCo/Ti-6Al-4V is about 2 - 4 J/m<sup>2</sup> for film thickness ranging from 1 μm to 8 μm.
3. The interface toughness of FeCo thin film on Ti-6Al-4V varies with location and interface decohesion tends to occur at the location with the lowest interface toughness.
4. Ion-cleaning of Ti surfaces can enhance the interface toughness and adhesion of FeCo thin film on Ti-6Al-4V.



5. The sequence of damage mechanisms in the FeCo thin films is the formation of microcracks in the thin films, followed by interface crack formation and propagation, and then detachment of thin film patches from the substrate.
6. The presence of thin FeCo films on Ti-6Al-4V has no effect on the fatigue life of the Ti-6Al-4V substrate in the low-cycle fatigue regime.
7. FeCo thin films are durable as magnetostrictive sensors. The overall durability of the FeCo thin films is in the range needed for practical application of the film as imbedded sensors.

Though not presented, experimental evidence in this study has also led to the conclusion that the presence of microcracks and interface debonds in the FeCo thin films did not affect the functionality of the sensor to detect strain via the inverse magneto-elastic effect.

### 3.5.6 References

- [1] K. S. Chan, S.J. Hudak, Jr., B.R. Lanning, C. Smith, A. Veit, and G.M. Light: "Durability of FeCo Thin Films on Ti-6Al-4V," *Metall. Mater. Trans. A*, 2005 (to submit).
- [2] M. D. Drory and J.W. Hutchinson: *Proc. R. Soc. London*, 1996, Vol. 452, pp. 2319-2341.
- [3] M-Y. He, A.G. Evans, and J.W. Hutchinson: *Int. J. Solids Structures*, 1994, Vol. 31, No. 4, pp. 3443-3455.
- [4] J. Dundurs: *J. Appl. Mech.*, 1969, Vol. 36, pp. 650-652.
- [5] K.S. Chan and M. P. Enright: *Metall. Mater. Transactions A*, 2005 ( in press).
- [6] Advanced High Cycle Fatigue Life Assurance Methodologies, UDR-TR-2003-00115, Final Report for AFOSR Contract F49620-99-C-0007, University of Dayton Research Institute, July 2004.